Master thesis

Topological phases and fermionic superfluidity on the Lieb lattice

Jeffrey C. Everts

Utrecht University
Institute for Theoretical Physics

August 21, 2012

Supervisors:

prof. dr. Cristiane de Morais Smith (UU)
dr. Vladimir Juričić (UL)
dr. Wouter Beugeling (UU)

Abstract

The Lieb lattice is an interesting lattice structure that can host interesting topological phases and novel fermionic superfluids. The fact that this two-dimensional lattice has three sites per unit cell, leads to three bands in the spectrum for tight-binding models. An intrinsic spin-orbit coupling term opens gaps between the three bands, which in addition, host a quantum spin Hall effect. The intricate nature of the multi-gap structure opens up the possibility to realize topological phase transitions driven by the next-nearest neighbour hopping t', which are accompanied by a change of spin Chern numbers of the various bands. We envisage a realization of such phenomena in optical lattices under shaking, where the ratio of t' to the next-nearest hopping t can be tuned to, in principle, any value. Finally, we will consider interaction-driven instabilities towards fermionic superfluidity on the Lieb lattice, with a special emphasis on systems with a point-like Fermi surface. Various types of possible superfluids will then be discussed.

Contents

Chapter 1

Introduction

Our main focus in this thesis will be the Lieb lattice: a two-dimensional square lattice with a basis that consists of three sites. It occurs for example in the the high-temperature tetragonal phases of the so-called cuprates: layered, ceramic materials that exhibit the phenomenon of high-temperature superconductivity. The sites in this lattice then play the role of the copper and oxygen atoms that provide the periodic potential in which the electrons can move. Moreover, it is believed that the superconductivity occurs in these layers. An example of a high temperature superconductor (HTSC) is given in Figure 1.1, where we also display the CuO planes that have the geometry of a Lieb lattice. Since the HTSCs are one of the prime motivations of studying this lattice, we feel it to be appropriate to sketch a few of its features in this introduction, although the topics in the next few chapters will not be directly related to the phenomenon of high-temperature superconductivity. However, some of the ideas that were proposed in the context of the cuprates will still be used to investigate various properties of the Lieb lattice. Here we are referring to the circulating current states proposed by C.M. Varma: states that break time-reversal symmetry, while leaving the discrete translational symmetry of the lattice intact.

1.1 A general view on the cuprates

It is remarkable that so many years after the discovery of the cuprates in 1986 by J.G. Bednorz and K.A. Müller [2], we still do not understand why these materials can become superconducting. Maybe this reflects the complexity of a problem at which possibly charge, spin, orbital and lattice degrees of freedom couple strongly with each other. Despite the complicated nature of these compounds, it did not take long until the charge carriers in the superconducting phase were identified as Cooper pairs [3], just like in the conventional superconductors that can be descibed by the microscopic theory of Bardeen, Cooper and Schrieffer (BCS) [4]. However, there is some evidence that unlike in BCS superconductors, the superconducting order parameter transforms non-trivially according to the point-group symmetry of the underlying lattice. One of the most convincing experiments that showed this was due to Tsuei *et al.* [5]. By using scanning SQUID magnetometry, they pointed out that the
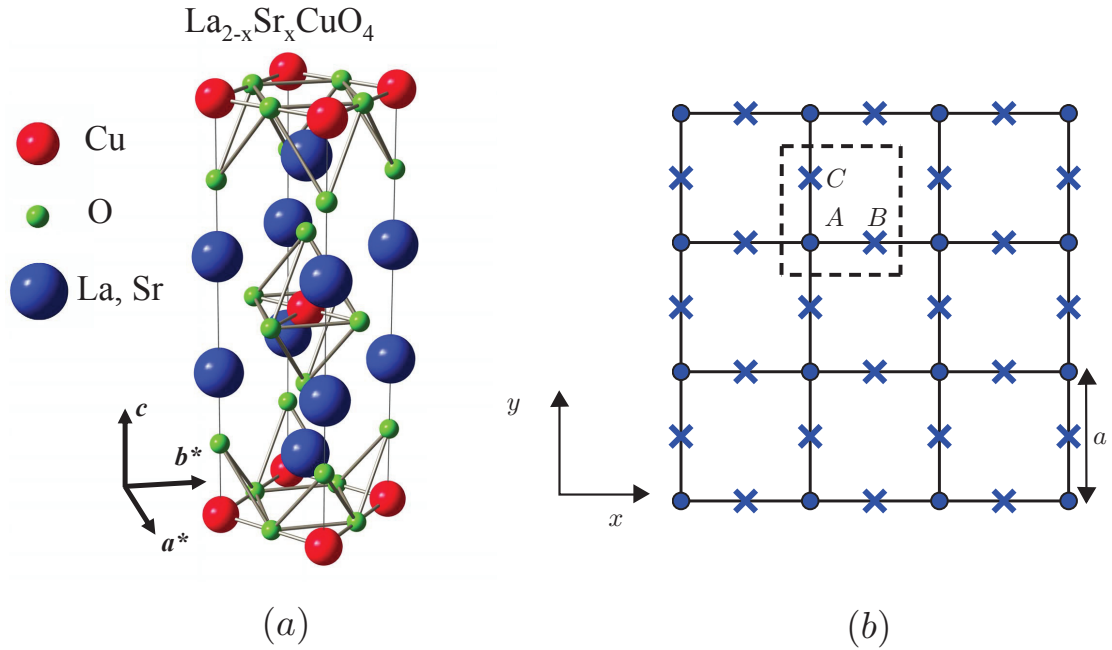
Figure 1.1: (a) Chemical structure of $La_{2−x}Sr_xCuO_4$ (LSCO), where the CuO layers have the geometry of the Lieb lattice. Figure adapted from Ref. [1]. (b) The unit cell of the Lieb lattice is indicated, together with the three sublattices A, B, and C.

cuprates are d-wave superconductors, instead of conventional s-wave superconductors. One of the consequences of such a pairing symmetry is the emergence of nodal quasiparticles, excitations that cost no energy, which can be seen in, for example, dynamical spin susceptibility or optical conductivity measurements [6]. However, the exact pairing symmetry is not a completely resolved issue yet, since there are still experiments contradicting this result [7].

Another subject of debate is the underlying pairing mechanism. The 'conventional' retarded phonon mediated interactions could not explain the high critical temperature T_c that was found in some of the cuprates, and for this reason many other pairing mechanism were proposed, such as a mediation by spin fluctuations, excitons or polarons. All these proposals literally pushed the BCS idea to its limits. However, knowing the exact pairing mechanism is just one of the necessities for BCS theory to work, the other being the occurrence of an instability within the Fermi surface. This just means that the normal state must be a Fermi liquid if we want to apply BCS theory. However, there is ample evidence that parts of the normal state in the phase diagram cannot be explained within this view [8]. Before touching this point, we need to explain the general phase diagram for the cuprates.

1.1.1 Structure and phases of the cuprates

A first look at the cuprates reveals a very complicated chemical structure, which is a possible reason why the physics of these compounds is difficult to understand. Besides their structural diversity and
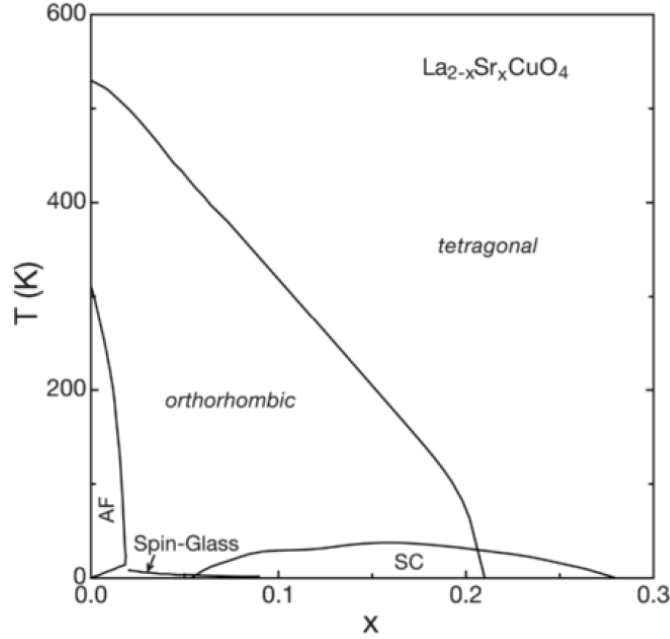
Figure 1.2: Phase diagram of LSCO as a function of doping. Figure adapted from Ref. [7].

complexity, there are also many similarities. All cuprates have CuO_2 planes, with the geometry of a Lieb lattice, which are separated by layers containing atoms like Ba, Tl, La, and O. The latter layers are often thought of as charge reservoirs: they provide the charge carriers to the CuO_2 planes, in which the superconductivity is believed to occur. Let us take $La_{2-x}Sr_xCuO_4$ (LSCO) as an example (see Figure 1.1 (a)). We observe that every copper atom is surrounded by six oxygen atoms in a distorted octahedral arrangement. It is not a perfect octahedron, since the bond length ($\sim$2.4 Å) of copper with an oxygen from the charge reservoir (the so called apical oxygen) is longer than that of a bond with an oxygen from the CuO_2 plane ($\sim$1.9 Å). The first type of bond is thus weaker than that of the in-plane Cu-O bonds, giving rise to the thought that the essential physics happens in the two-dimensional CuO_2 planes.

In the undoped regime, all cuprates are anti-ferromagnetic Mott insulators: materials that are insulators because of interactions. A superconducting region is formed upon doping above a critical value x_c. The parent compounds are doped upon the insertion of substitutional or interstitial impurities, resulting in either fewer electrons donated to the CuO_2 planes (the material is then called hole-doped or p-doped) or an excess of electrons (called electron-doped or n-doped). The critical temperature T_c of the superconducting regime is first increased by adding dopants, this region is called underdoped. After a while T_c decreases upon increasing doping, this region of the superconducting dome is called overdoped. The regions for which T_c is around its maximum is called optimally doped.

A typical phase diagram as function of doping is shown in Figure 1.2 for $La_{2-x}Sr_xCuO_4$ (LSCO), a hole-doped cuprate. Replacing La^{3+} randomly by Sr^{2+} results in fewer electrons donated to the CuO_2 planes. This introduces holes in these layers and this fact is supported by measurements of the sign of the Hall coefficient. After the material is sufficiently doped, it exhibits a superconducting

phase (SC), preceded by a spin glass phase, as shown in the phase diagram of Figure 1.2. The critical temperature is about 40 K when optimally doped. At sufficiently high temperatures, there is a phase transition from the superconducting state to the normal state. Finally, we observe that there is also a structural phase transition in this material, from a high-temperature tetragonal phase to a low temperature orthorhombic structure. This structural phase transition is accompanied by the tilting of the octahedra, effectively elongating the crystal in certain directions.

Remarkably, the concept of doping occurs in all the cuprates. There are, however, some differences. For example, in the hole-doped cuprate $YBa_2Cu_3O_{7-x}$ (YBCO), the optimally doped material has a much higher T_c than LSCO (~ 92 K). This could be attributed to the fact that this material has two CuO_2 layers instead of a single layer between subsequent charge reservoirs. There are also structural differences: YBCO is characterized by having small CuO chains in the charge reservoir, that are absent in LSCO. These affect some properties, such as the optical conductivity. From this discussion, it should be clear that there are some differences among the HTSCs, but in the rest of the thesis we will only focus on the properties that are common to most of the cuprates. For this, we are going to have a closer look at generic features of the phase diagram.

1.1.2 Properties of the normal state in high-temperature superconductors

A careful look at the phase diagram for LSCO in Figure 1.2 already shows a richer structure than in the BCS superconductors. For example, the material at zero doping (the so-called parent compound) is a Mott insulator. The general view on this is that the strong Coulomb repulsion U on the Cu sites is large enough to restrict the motion of the charge carriers at half filling (i.e. one electron per Cu site). Metaphorically, it is as if the electrons are in a complete stand-still, just like cars in a traffic jam [9]. In this view, the oxygen atoms in the CuO layers are most often neglected. If we would take them into account however, the cuprates are better characterized as being charge-transfer (CT) according to the Zaanen-Sawatzky-Allen scheme [10]. The difference is that the motion of charges is not restricted by the large U, but by the charge-transfer energy Δ_{pd} between the orbitals of Cu and O. Because $\Delta_{pd} < U$, there is a CT band composed mainly of oxygen orbitals, that lies between the upper and lower Hubbard band [11]. At half-filling, the system is filled up to this band, meaning that the doped holes will mainly reside on the O sites. However, in n-doped materials the electrons will mainly reside on Cu sites.

The phase diagram of LSCO shown in Figure 1.2 does not reveal the full complicated structure of the normal state. Lead by measurements of transport properties (e.g. electrical resistivity), thermodynamic properties (e.g. heat capacity, magnetic susceptibility), structure (in the spin or charge sector with the help of neutron scattering, scanning tunneling microscope (STM) or angle-resolved photoemission spectroscopy (ARPES)) or some other spectroscopic properties (such as the Knight shift in nuclear magnetic resonance (NMR) spectroscopy, or Raman spectroscopy), we can draw additional lines in the phase diagram for the cuprates. A particular view is shown in Figure 1.3, where the 'normal' phase is split into three regions. However, different experiments yield different lines in the phase diagram, so the distinction between the mentioned regions is not well-defined. In other words, the transition between these various regions are not sharp and should be seen as cross-overs.
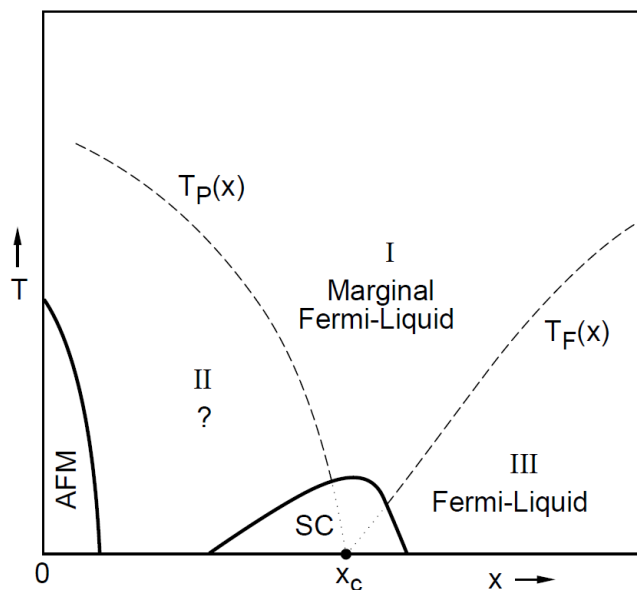
Figure 1.3: Generic phase diagram for hole-doped cuprates. Specific features found for some of the cuprates are omitted, such as a spin glass phase. Figure adapted from Ref. [12].

Moreover, different experiments probe different length and/or time scales. Also, some techniques are surface based (e.g. STM or ARPES), while others measure bulk properties (e.g. neutron scattering). Some experiments probe order in real space (e.g. STM), while others probe order in momentum space (e.g. ARPES). This makes the comparison between the different experiments very difficult. Finally, not many types of cuprates are easily synthesized in the whole doping range of interest, making comparisons between different materials difficult.

Let us now investigate each of the regimes in the normal state in more detail. In the far overdoped regime, the normal state behaves like a Fermi liquid. In this region, if the temperature is sufficiently low, there are only quasiparticles. This results in an in-plane resistivity which scales with temperature like $\rho \sim T^2$ at low temperature. Instead, close to the optimally doped regime, the linear resistivity scales linearly with temperature for sufficiently low T. Another unusual feature of the resistivity is the large anisotropy associated with it. The temperature dependence of the resistivities in-plane are different from the resistivity perpendicular to the Cu-O planes. These experiments suggest that the charge carriers move indeed in the Cu-O planes, as it was mentioned before, but that they tend to localize in the direction perpendicular to these planes. Finally, it is known that the Hall coefficient in this region is strongly temperature dependent. Because of this behaviour, region I in Figure 1.3 is called 'strange metal' or marginal Fermi liquid (MFL).

In the MFL region of the phase diagram, it is believed that the concept of a quasiparticle is lost. Ideas about quantum criticality are very popular in the theoretical community to explain the properties of this part of the phase diagram. The linear resistivity can then be explained by the fact that the current is carried by quantum fluctuations, which appear because of the close proximity to a quantum critical point (QCP), see Figure 1.3. A QCP denotes the occurrence of a second order phase transition
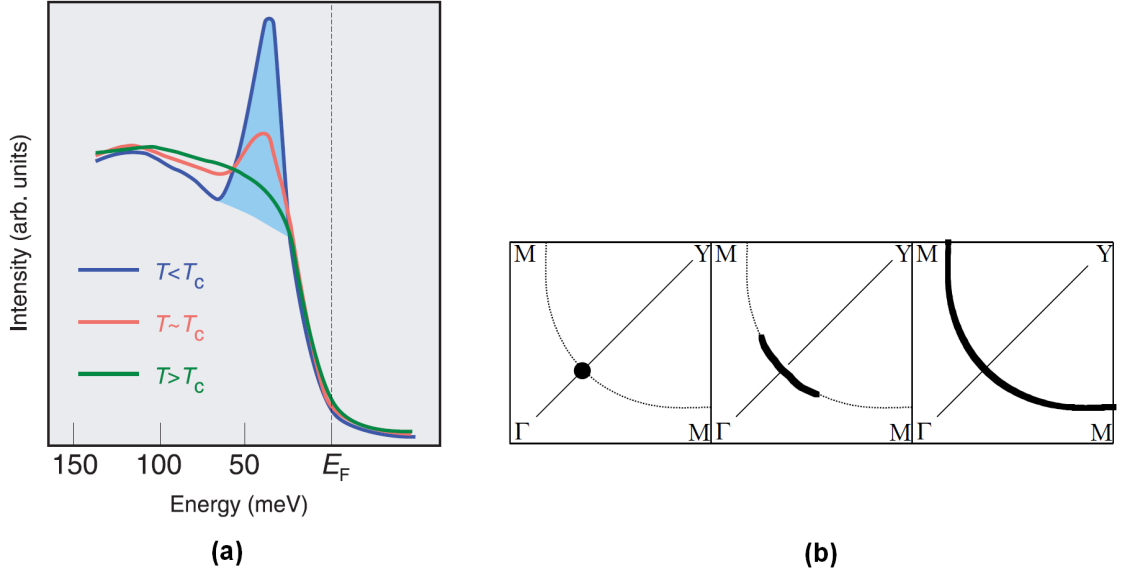
Figure 1.4: (a) Representation of ARPES spectra for underdoped cuprates at an antinodal point. Below T_c a well-defined quasi-particle peak is observed, which disappears when raising the temperature. Notice that a gap persists for all T. Figure adapted from Ref. [14]. (b) Evolution of the Fermi surface upon raising the temperature. Below T_c (left panel) a d-wave node exists, which evolves into a gapless Fermi arc above T_c (middle panel). When the four Fermi arcs meet, a fully connected Fermi surface is formed (right panel). Figure adapted from Ref. [15].

at $T = 0$. This emphasizes the role of quantum fluctuations in this phase transition, as thermal fluctuations are absent at this point. Note that a QCP is difficult to detect, since its appearance may be obscured by the presence of superconductivity.

Maybe the most complicated part of the normal state is the region with a question mark. In this region, an anisotropic loss of states in the single particle excitation spectrum is observed, even though the material is not superconducting. This is called the pseudogap phase and is one of the most intriguing features of the cuprates. The presence of the pseudogap expresses itself in NMR measurements of the Knight shift, Raman scattering, neutron scattering, but also in transport measurements such as the electrical resistivity [13].

The number of experiments performed in the pseudogap regime is vast. Many unconventional features are observed in this part of the phase diagram [7, 13]. Here, we will shortly discuss some observations done with ARPES. In ARPES, the photoemission intensity at fixed momentum is measured, which is roughly equal to the probability of finding an electron at a given momentum and energy. When spectra are recorded in the SC phase at a point of the Brillouin zone where the d-wave gap is maximal, at the so-called antinodal point, we observe spectra as shown in Figure 1.4 (a). The intensity is low above the Fermi energy, which indicates the presence of a gap. Moreover, below T_c, a peak is observed in the spectrum which corresponds to a quasiparticle, a well-defined electronic excitation. Upon raising the temperature, the peak becomes smaller and ultimately disappears, while

the gap remains. This is an indication that quasiparticles may be absent in the pseudogap phase. In contrast, far in the overdoped region (not shown), the gap disappears above T_c, but there is still a quasiparticle peak. The disappearance of a quasiparticle peak is also observed in the MFL region of the phase diagram.

Another interesting feature of the pseudogap region can be seen when the electronic dispersion is probed as a function of momentum. In the SC regime, there is a gap everywhere except at the nodal points in momentum space, because of the d-wave nature of the superconductor. When the temperature is raised above the critical temperature, these so-called Fermi points are replaced by Fermi arcs. These arcs eventually grow until they meet each other and form a connected Fermi surface (Figure 1.4(b)). Here it becomes clear why it is difficult to understand the nature of the pseudogap. As of now there exists no framework to handle electronic systems without a well-defined Fermi surface. Nevertheless, there are many theories proposed to describe the nature of the pseudogap.

One of the earliest ideas about this subject is that the occurrence of a pseudogap is an indication that preformed Cooper pairs develop [16], or stated differently, that it has to do with a form of fluctuating superconductivity. Here, it is argued that it is possible that phase coherence occurs at a later stage than the formation of the Cooper pairs. This needs to be contrasted with the conventional superconductors, for which BCS theory assumes that pairing and phase coherence occur at the same point in the phase diagram, namely at T_c. Although the idea is relatively old, it still finds some recent experimental support [17].

Another popular idea is that the pseudogap phase is accompanied by many types of order which compete with each other. The idea of competing, hidden order in the pseudogap phase makes the various ordering mechanisms in the cuprates at least as rich as the ones observed in the field of soft condensed matter. In this research area, various inhomogeneous structures are well known, such as those found in copolymer blends or in self-assembling concentrated amphiphilic solutions [18]. In contrast to what is found in soft matter physics, in the cuprates it is the electrons that may order in an inhomogeneous fashion and not the molecular constituents. In addition, most of the proposed orders have experimental evidence, suggesting that various types of order may compete and even coexist with each other. Another unclear aspect is whether they favor or compete against superconductivity. This makes the pseudogap region the playground of many exotic ordering phenomena. Notable examples are various forms of charge segregations, such as the the stripes discovered by Zaanen and Gunnarson [19] (for a review on stripe physics see [20]), quantum liquid crystals or the resonating valence bond (RVB) state proposed by Anderson [21]. However, we will only focus on yet different proposals: the so-called spontaneous diamagnetic currents. This is because we will use them as inspiration to investigate various properties of the Lieb lattice in this thesis later.

1.2 Mesoscopics of the pseudogap phase: spontaneous diamagnetic currents

Before we can discuss the spontaneous diamagnetic current phases, we have to discuss the models that are used in this context. Most of the models that are trying to describe the behaviour of the

cuprates, focus their attention on the CuO$_2$ planes. It is believed that the comprehension of the physical properties of these two-dimensional systems is essential for understanding the mechanism triggering superconductivity in the cuprates. At the end, it may be necessary to couple these layers to each other because in two dimensions it is not possible to find true long range order via a spontaneously broken continuous symmetry. This fact follows from the Mermin-Wagner-Hohenberg theorem [22, 23]. Notice that it is essential that the symmetry to be broken is continuous, showing why this theorem does not apply, for instance, to the two-dimensional Ising model.

1.2.1 Electronic models

A very popular way to model the CuO$_2$ planes is by using the tight-binding approach combined with an on-site Coulomb repulsion. The latter is taken into account because we know, for example, from LSCO, that the undoped material is a Mott insulator. In such a model only the highest occupied orbitals of Cu and O are taken into account. Due to the underlying lattice structure, the degeneracy of the d orbitals of Cu is lifted, such that the highest occupied orbital is of $d_{x^2-y^2}$ character. For oxygen these are the p_x and p_y orbitals. If one defines the vacuum to be the state for which Cu and O attain their closed-shell configuration, we can define fermionic creation (annihilation) operators $\hat{p}^\dagger_{j,\sigma}$ ($\hat{p}_{j,\sigma}$) that create (destroy) a hole with spin σ on a p orbital of oxygen on site j. Similarly, this can be done for a d orbital of Cu, for which we will denote the creation (annihilation) operator for a hole with spin σ on site i by $\hat{d}^\dagger_{i,\sigma}$ ($\hat{d}_{i,\sigma}$). Then it is possible to write down a Hamiltonian $\hat{H}_{3B}$

$$\hat{H}_{3B} = - t_{pd} \sum_{\langle ij \rangle, \sigma} \left(\hat{p}^\dagger_{j,\sigma} \hat{d}_{i,\sigma} + \text{h.c} \right) - t_{pp} \sum_{\langle jj' \rangle, \sigma} \left(\hat{p}^\dagger_{j,\sigma} \hat{p}_{j',\sigma} + \text{h.c} \right) + \epsilon_d \sum_{i,\sigma} \hat{d}^\dagger_{i,\sigma} \hat{d}_{i,\sigma}$$
$$+ \epsilon_p \sum_{j,\sigma} \hat{p}^\dagger_{j,\sigma} \hat{p}_{j,\sigma} + U_d \sum_i \hat{d}^\dagger_{i,\uparrow} \hat{d}_{i,\uparrow} \hat{d}^\dagger_{i,\downarrow} \hat{d}_{i,\downarrow} + \frac{U_p}{2} \sum_j \hat{p}^\dagger_{j,\uparrow} \hat{p}_{j,\uparrow} \hat{p}^\dagger_{j,\downarrow} \hat{p}_{j,\downarrow}$$
$$+ V_{dp} \sum_{\langle ij \rangle, \sigma} \hat{d}^\dagger_{i,\sigma} \hat{d}_{i,\sigma} \hat{p}^\dagger_{j,\sigma} \hat{p}_{j,\sigma} + V_{pp} \sum_{\langle ij \rangle, \sigma} \hat{p}^\dagger_{i,\sigma} \hat{p}_{i,\sigma} \hat{p}^\dagger_{j,\sigma} \hat{p}_{j,\sigma}. \tag{1.1}$$

This model is called the Emery model [24] or simply the three-band Hubbard model, because we have three orbitals in a unit cell with Hubbard-like interactions, see Figure 1.5. It takes into account the hybridization between nearest neighbour Cu and O atoms by a hopping parameter t_{pd}. Moreover, a O-O hopping term is included with parameter t_{pp}. The on-site energies for occupying a $2p$ ($3d$) orbital is given by ϵ_p (ϵ_d). The strong on-site (Coulomb) repulsion when two holes occupy the same $2p$ ($3d$) orbital is taken into account by the parameter U_p (U_d). Nearest-neighbour Coulomb repulsion is taken into account by V_{pd} and V_{pp}. At half-filling (one hole per site, meaning no dopant) and in the strong-coupling regime, the model reduces to a Heisenberg model with a superexchange [1] antiferromagnetic coupling. This is just as we expect, because it is known that the Heisenberg model provides a good description of the undoped cuprates.

It did not take long before an effective Hamiltonian for the three-band model was written down, which only took into account the copper sites (although it is still controversial whether this is allowed). This idea was pointed out by F. C. Zhang and T. M. Rice [26]. They showed that the hybridization

---

[1]This is called superexchange because it is a coupling of the copper cations through a non-magnetic oxygen anion.
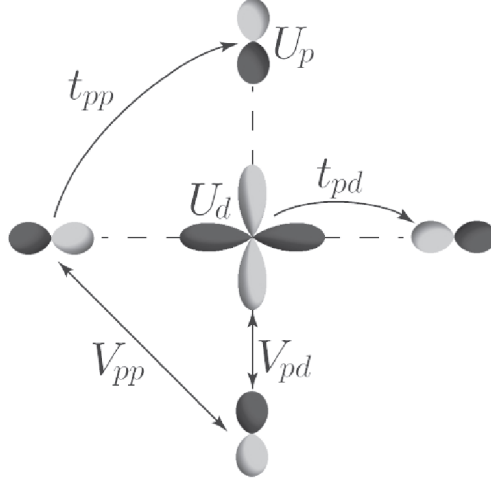
Figure 1.5: Unit cell for the desciption of CuO_2 planes in the Emery model. The various hopping and interaction paramters are shown, together with the orbital degrees of freedom that are taken into account of Cu $\left(d_{x^2-y^2}\right)$ and O (p_x, p_y). Figure adapted from Ref. [25]

strongly binds a hole on each square of O atoms to the central Cu^{2+}, to form a local singlet. This so called Zhang-Rice singlet (with $S = 0$) is equivalent to removing a spin on a copper site, such that the effective theory described holes (the spin singlets) on a square lattice of copper spins. The effective Hamiltonian for such a system is the $t - J$ model,

$$
\hat{H}_{t-J} = J \sum_{\langle ij \rangle} \left(\hat{\mathbf{S}}_i \cdot \hat{\mathbf{S}}_j - \frac{1}{4} \hat{n}_i \hat{n}_j \right)
$$
$$
- t \sum_{\langle i,j \rangle; \sigma} \left[\hat{c}^\dagger_{i,\sigma} (1 - \hat{n}_{i,-\sigma})(1 - \hat{n}_{j,-\sigma}) \hat{c}_{j,\sigma} + \text{h.c.} \right].
\tag{1.2}
$$

Here, $\hat{\mathbf{S}}_i$ denotes the spin-$1/2$ operators at sites i for the square lattice of copper and J is the antiferromagnetic nearest-neighbour coupling. Every site in this model can have three possible states, namely a Cu $3d$ hole with spin up or down, or a singlet state which corresponds to an empty site. The terms on the second line describe the hopping of the $3d$ holes on the lattice without changing their spin, for which double occupancy is forbidden by the projection operator $1 - \hat{n}_{i,-\sigma}$. Finally, we see that the $t - J$ model is actually equivalent to another much studied model in the field of high-temperature superconductivity, namely the single-band Hubbard model with Hamiltonian $\hat{H}_{\text{hub}}$

$$
\hat{H}_{\text{hub}} = -t \sum_{\langle i,j \rangle; \sigma} (\hat{c}^\dagger_{i,\sigma} \hat{c}_{j,\sigma} + \text{h.c.}) + U \sum_i \left(\hat{n}_{i,\uparrow} - \frac{1}{2} \right) \left(\hat{n}_{i\downarrow} - \frac{1}{2} \right),
\tag{1.3}
$$

in the limit of strong on-site repulsions U. This model was proposed by Anderson to describe the essential physics of the cuprates [21].
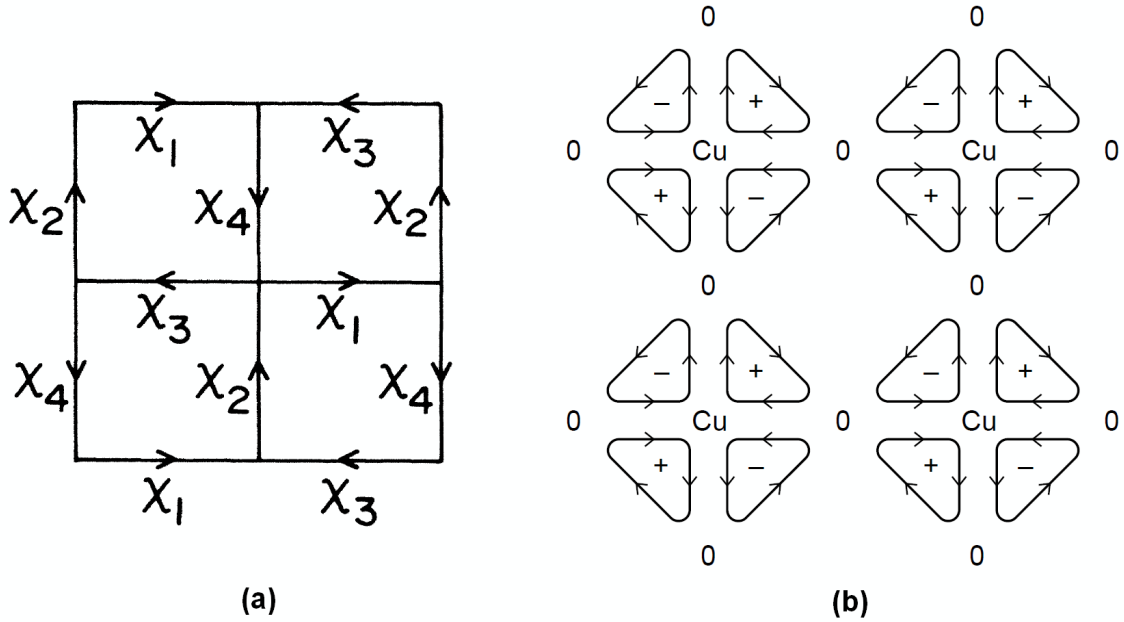
Figure 1.6: (a) Staggered currents for the DDW order and staggered π-flux phase. Only the Cu sites are taken into account. Every plaquette has a flux of $\pm\pi$. Picture adapted from Ref. [27]. (b) Circulating currents as proposed by Varma. Picture adapted from Ref. [12].

1.2.2 Staggered π-flux phase and d-density wave order

Let us first consider the $t - J$ model. When treated in mean-field, a special solution was found by Kotliar [28] and independently by Affleck and Marston [29], which was called the staggered π-flux phase. This solution is described by a complex hopping parameter between the various Cu sites (the oxygen atoms are not taken into account) with a phase chosen such that there are staggered orbital currents flowing around plaquettes in the Cu planes, see Figure(1.6)(a). This induces a flux of $\pm\pi$ in every plaquette, hence the name staggered π-flux phase. These currents give rise to alternating small moments, which are difficult to detect experimentally [30]. This phase breaks parity, time-reversal, translational and rotational symmetries.

The energy dispersion of the π-flux phase shows many interesting features. It exhibits an energy gap, as it should for describing the pseudogap regime. Interestingly, this gap vanishes at the nodal points located at $(\pm\pi/2, \pm\pi/2)$. At these points Dirac cones emerge, meaning that the dispersion increases linearly around these points [31]. Finally, we remark that the emergence of a π-flux phase can be put in a more general context of gauge theories (such as $SU(2)$), where it is believed that this phase emerges upon doping, since in that case the gauge invariance is lifted [31].

The idea of staggered fluxes was put into a more general setting by Nayak [32]. He proposed that the occurrence of staggered fluxes is a natural consequence of the appearance of d-wave superconductivity in the cuprates. By imposing an order parameter with d-wave symmetry, he showed that the competition with other order parameters was able to describe some of the features of the pseudogap phase [33]. If one would have imposed s-wave symmetry, the same order parameter would describe

charge density waves (CDW). Hence, this type of order was called d-density wave (DDW). The DDW order breaks parity, time-reversal, translational and rotational symmetries, because also here the alternating current patterns gives rise to magnetic moments. As of now, however, this type of order has no experimental evidence.

1.2.3 Circulating current phases

One of the main assumptions of the staggered flux phase and DDW order is that the oxygen atoms are not taken into account to describe the CuO planes. Chandra Varma, however always believed that the oxygen atoms cannot be neglected. By doing a suitable mean-field coupling of a three-band Hubbard model, he proposed a phase similar to the currents found in the DDW order [12]. However, here the orbital currents flow around O-Cu-O plaquettes. An example of such a circulating current (CC) phase or Varma phase is shown in (Figure 1.6(b)). With this construction, Varma could explain some of the features in the pseudogap phase. Moreover, the fluctuations in the order parameter that provide these orbital currents could be used as a pairing mechanism to get d-wave superconductivity at a sufficiently low temperature [34]. Finally, we note that Varma's construction heavily relies on the existence of a QCP. This is in contrast to Anderson's RVB picture, where the pseudogap is proposed to be the result of fluctuations towards a d-wave superconductor.

Because of the more involved lattice geometry when oxygen is taken into account, there are several possibilities for the orbital currents to flow. We will see various possibilities in this thesis. However for now, we note that the Varma phase is unique in that it only breaks time-reversal symmetry, but leaves the symmetry of the lattice intact, giving experimentalists a handle for detecting this type of order. Recent experimental results by the group of Bourges [35] and somewhat later by the group of Kapitulnik [36] provide support for this type of order.

From the discussion above, it should be clear that there are many interesting proposals to explain the rich phenomena in the cuprates. In these proposals, the Lieb lattice geometry may play an important role. In this thesis, we will investigate the Lieb lattice simply because it is an interesting lattice structure to study, with a possible realization as an optical lattice. We will focus on topological properties and on instabilities towards fermionic superfluidity for a given band structure.

1.3   Outline of this thesis

Now that we have a clear motivation in mind, we will go to the main subjects in the thesis. First of all, we will discuss various topological states of matter that a Lieb lattice can host. To fully appreciate this, we will first introduce the concept of a topological insulator (TI) in Chapter 2. We will see how topological invariants can relate bulk properties to distinct edge properties and how these type of materials cannot be adiabatically connected to conventional states of matter. Various discrete symmetries play an important role here. Then we will put the Varma phases in a topological perspective, by discussing the work by Sun and Fradkin [37] and He *et al.* [38]. Moreover, since we will be mostly interested in the non-interacting case in the tight-binding regime, we will also discuss a possible experimental

realization of TIs in optical lattices.

In Chapter 3, we will start discussing our own contribution to the field of TIs. Elaborating on the work done by Weeks and Franz [39] for the Lieb lattice, we find that a real next-nearest-neighbour hopping can drive many interesting topological phase transitions in a model that accounts for an intrinsic spin-orbit coupling term. Moreover, we will see that our construction is equivalent to two copies of one of the Varma phases. Finally, we will discuss the requirement of having multiple gaps for realizing these topological phase transitions.

Chapter 4 will be concerned about interaction-driven instabilities on the Lieb lattice, treated on a mean field level in the particle-particle channel. Conventionally, these states of matter are known as superconductors, but in our case it is more accurate to name them fermionic superfluids. This is because we will think about possible realizations in optical lattices and these set-ups necessarily host neutral particles instead of electrons. Moreover, we will assume that there is already an attractive interaction between the particles and we will ask ourselves the question how the emergent quasiparticles from a tight-binding band structure could pair. Because of the complexity of this problem. we will only lay down the framework for studying these phenomena on the Lieb lattice. We will leave various numerical studies for a future work. Finally, we will conclude in Chapter 5 and we will provide an outlook for future research.

Chapter 2

Topological quantum matter

The field of topological insulators and topological superconductors received much attention in the last decade. These types of quantum matter have a bulk that is insulating or superconducting, while the edge or surface of the sample hosts topologically protected gapless modes. The protection is a result of the fact that these materials cannot be adiabatically connected to a state of matter that is topologically trivial. For example, we can imagine that these systems are described by a Bloch Hamiltonian that depends on a set of parameters, such as coupling constants or hopping amplitudes. By tuning these parameters slowly enough in time (i.e. adiabatically) the gapless modes cannot disappear without a band gap closing. This property makes these systems very interesting for various applications, such as novel spintronic devices or topological quantum computing.

In this chapter, we will make these ideas more precise, by discussing the quantum Hall effect in various forms and the quantum spin Hall effect. We will restrict our discussion only to system where the concept of a band structure applies and we will highlight the necessary concepts from topological band theory that we will need in Chapter 3. Essentially, this means that we are only going to Hamiltonians with single-particle like terms. This includes the non-interacting case, interactions that can be written in a single particle picture (e.g., spin-orbit coupling), or interactions treated in mean-field. We conclude with a possible experimental realization of topological quantum matter using cold atoms. For a more thorough discussion of topological quantum matter, that for example includes a discussion about topological field theory, we refer to Ref. [40]. Another excellent review for topological insulators can be found in Ref. [41].

2.1   A topological view on the integer quantum Hall effect

The integer quantum Hall effect (IQHE), discovered by Von Klitzing *et al.* [42] in 1980 and first theoretically predicted by Ando *et al.* in 1975 [43] , is the first example of topological quantum matter found in history. Indeed, it was one of the first instances where the concept of spontaneous symmetry breaking and hence the concept of an order parameter in the conventional sense did not apply.

In principle, the experiment is very simple. We start out with a thin slab of semiconducting (or insulating) material, such as a GaAs heterostructure, for which the length and width are much larger
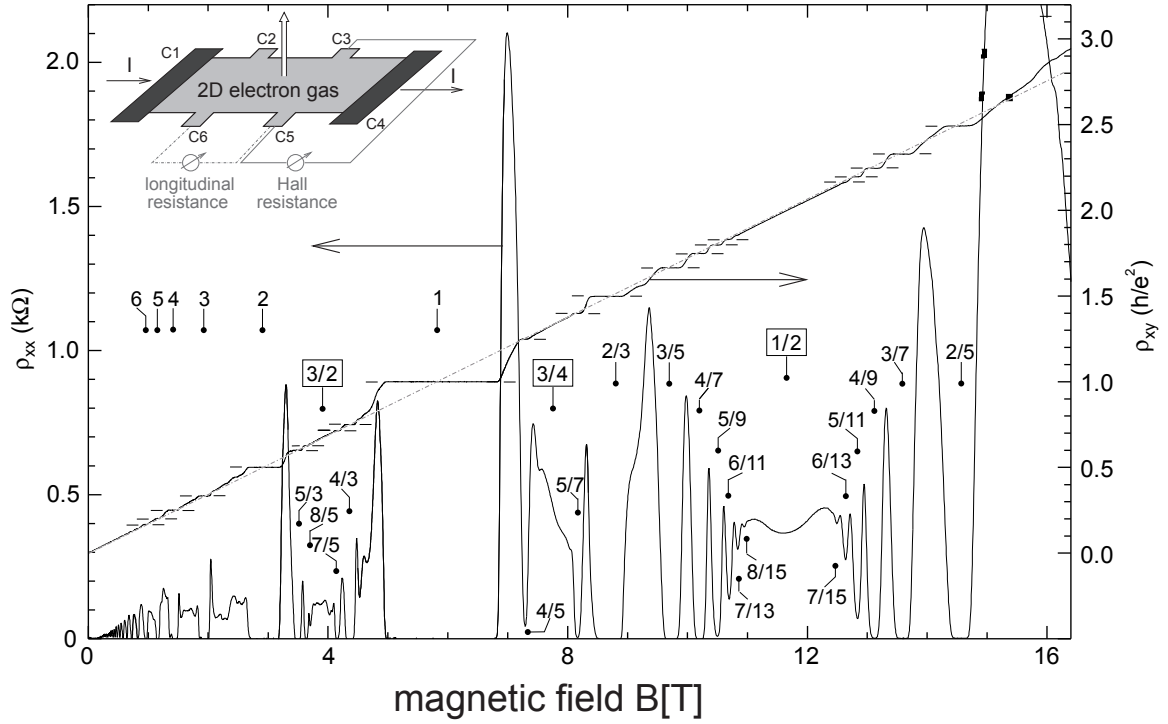
Figure 2.1: Typical measurement of the IQHE and FQHE as performed by J.Smet, MPI-Stuttgart. The experimental set-up is shown in the upper left corner. The dashed-dotted line indicates the classical Hall response. At sufficiently low temperatures plateaus start to form in the transverse resistance as a function of B. The numbers indicate the filling fractions n, the integer ones are for the IQHE, the fractional ones for the FQHE. The peaks in longitudinal resistance were not discussed in the text, but are the result of the formation of a percolating network between the two current carrying edges for a suitable n. Figure adapted from Ref. [44].

than the height, so that the slab can essentially be seen as being two-dimensional. This slab is placed in an external magnetic field perpendicular to the surface area and subsequently the transverse conductance is measured perpendicular to the direction of the electric field. Normally, the classical Hall response is found: a transverse conductance σ_{xy} that is proportional to the norm of the magnetic field B. Such measurements are for example used to determine the type of charge carriers (electrons or holes). At sufficiently low temperatures, the semiconductor becomes insulating because of a lack of thermal excitations. However, the transverse conductance still persists, but with the remarkable observation that plateaus are formed in σ_{xy} as s function of B, see Figure 2.3. What is more remarkable is that these plateaus always occurred at an exact integer multiple n of the quantum of conductance, i.e., $\sigma_{xy} = ne^2/h$. Furthermore, it has been found that the entire contribution to this effect was from charge currents situated on the edge of the sample. These so-called edge states are chiral, which means that they are uni-directional.

At the time, it was believed that one of the essential ingredients for this to occur was the two-dimensionality and the time-reversal symmetry breaking by an external magnetic field. In such a set-up, we get the well-known orbital quantization of the spectrum in terms of Landau levels and it has been found that the integer n is related to the filling fraction of these energy levels. In systems where electron-electron interactions play an important role, n can also become a rational fraction, which leads to the so-called the fractional quantum Hall effect (FQHE) [45], also shown in Figure 2.3. However, as mentioned in the introduction, we will not discuss interacting systems beyond the mean-field level, so we will not touch upon the FQHE further than mentioning it.

Many explanations for the existence of chiral edge states in the IQHE exist. One is that they are the result of the skipping motion of the orbital electrons in the Landau levels against the edge of the sample. Another very appealing explanation emerges from the concept of topological invariants, and this will be of the most interest to us in this thesis.

Thouless, Kohmoto, Nightingale and Den Nijs [46] found in 1982 by a Kubo formula calculation that the filling fraction n is related to an integer topological invariant called the first Chern characteristic class, or simply Chern number, which in the context of the IQHE is also known as TKNN invariant, named after their discoverers. The Chern number for the α-th band (Landau level) is defined according to

$$\mathcal{C}_\alpha = \frac{1}{2\pi} \int_{(M)BZ} d^2\mathbf{k} F_{xy}^\alpha. \tag{2.1}$$

This formula is expressed as the integral over the (magnetic) Brillouin zone ((M)BZ) of the so-called Berry curvature F_{xy}^α, defined via the Berry connection A_μ^α according to $F_{xy}^\alpha = \partial_x A_y^\alpha - \partial_y A_x^\alpha$. Here, the Berry connection can be calculated from the eigenstates of the Hamiltonian $|\Omega_\alpha\rangle$ via the formula $A_\mu = -i\langle\Omega_\alpha|\partial_\mu|\Omega_\alpha\rangle$, where ∂_μ is a shorthand notation for the derivative with respect to k_μ for $\mu = x, y$. Notice that the Chern number is a property of the bulk bands and it can be shown that it can only take integer values. In this sense, it seems like another well-known topological invariant, namely the Euler characteristic which is a quantity that depends on the genus, or number of holes of a surface. It can be expressed via the Gauss-Bonnet theorem as the integral of the Gaussian curvature over a compact Riemannian manifold. This gives a simple way of relating local properties (curvature) to global properties (genus). However, for the Chern number there is not always such an intuitive explanation. Finally, we remark that the Chern numbers for the various bands are only well-defined if there are no band touching points.

Having a closer look at Eq. (2.1), we notice that the Chern number is actually equivalent to the Berry phase divided over 2π evaluated around a closed loop that encircles the BZ. This geometrical phase factor arises naturally in the cyclic adiabatic evolution of a quantum-mechanical system, in addition to the well-known dynamical phase factor [47]. One of the most important properties of the Berry phase factor is that it is gauge-invariant and hence observable. These properties give rise to many interesting effects on electronic properties [48].

However, we can see the Chern number also in a more differential geometric setting [49]. We can think of mappings of the 1BZ, which is topologically equivalent to a 2-torus $\mathbb{T}^2$, to the Hilbert space of Bloch Hamiltonians. By using the Bloch wave functions, a principle U(1) fiber bundle can be constructed on the torus and this defines a connection, the so-called Berry connection. With a

connection, we can define a curvature and hence define a Chern number.

We can finally ask ourselves the question of how a bulk property, such as the Chern number, is related to a property on the edge, namely the quantum Hall conductivity. This is by virtue of the bulk-boundary correspondence

$$n = \sum_{\alpha:\epsilon_\alpha < \epsilon_F} \mathcal{C}_\alpha, \tag{2.2}$$

and this states that the TKNN invariant just equals the sum of the Chern numbers of the filled bands. To show how this idea works in practice, we will consider another type of QHE, proposed by Haldane [50]. This will make the idea of the above correspondence more transparent, because the concept of Landau levels is not needed for such an explanation.

2.2   Quantum Anomalous Hall effect and bulk-boundary correspondence

At the time when the IQHE was discovered, it was believed that the essential ingredients for a QHE were two-dimensionality and time-reversal symmetry breaking by the presence of a magnetic field. Now we understand that both conditions are not necessary, but let us focus on the latter condition, assuming that we are in two space-dimensions. In 1988, Haldane proposed a theoretical model on the honeycomb lattice (graphene) to show that it can support a QHE without the application of an external magnetic field. For this reason it is also known as the quantum anomalous Hall effect (QAHE) or Haldane phase [50].

The construction of the model is as follows. Although no net magnetic field is present, Haldane allowed the magnetic flux to fluctuate in the lattice, but under the condition that there is no net flux through a unit cell. This means that there is still time-reversal symmetry breaking, but no Landau levels. This makes the QAHE effect an ideal example for explaining the bulk-boundary correspondence discussed in the previous section, because of its simplicity. Moreover, the 2×2 Hamiltonian matrix can be compactly written as

$$\mathcal{H}(\mathbf{k}) = \mathbf{d}(\mathbf{k}) \cdot \boldsymbol{\sigma}, \tag{2.3}$$

where $\boldsymbol{\sigma}$ is a vector of Pauli matrices. If we normalize the two component vector $\mathbf{d}$ and call this $\hat{\mathbf{d}}$, $\hat{\mathbf{d}}$ then can be seen as mappings from $\mathbb{T}^2$ (the 1BZ) onto the 2-sphere S^2. Because the Hamiltonian has this form, the Chern number has a simple interpretation as a winding number of $\hat{\mathbf{d}}$ over S^2,

$$\mathcal{C}_\pm = \pm \frac{1}{4\pi} \int_{1BZ} d^2\mathbf{k}\, \hat{\mathbf{d}}(\mathbf{k}) \cdot \left(\frac{\partial \hat{\mathbf{d}}}{\partial k_x} \times \frac{\partial \hat{\mathbf{d}}}{\partial k_y} \right), \tag{2.4}$$

where the plus (minus) sign refers to the upper (lower) band. Notice that this construction is not unique for the Haldane model, because it in principle holds for any $\hat{\mathbf{d}}$ vector. We can imagine that this object depends on a set of parameters, and with this formula it is easy to map out all the possible Chern numbers as a function of these parameters without calculating any eigenvectors. Finally, notice that the sum of Chern numbers of all the bands is always zero and indeed this property holds generally also for multiband models.
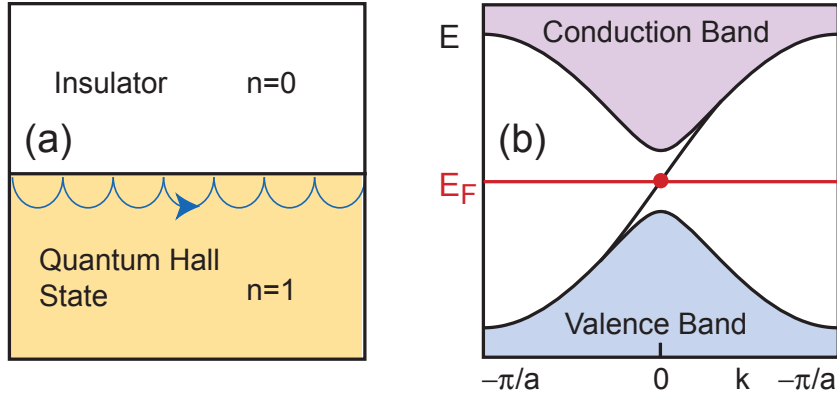
Figure 2.2: Schematic figure showing the QAHE. In (a) we observe the presence of a chiral edge state by connecting a non-trivial material with $n = 1$ with a trivial vacuum. (b) This edge state can be visualized in the spectrum by solving for a semi-infinite geometry. Figure adapted from Ref. [41].

Now, let us assume that for a certain set of parameters, the model in Eq. (2.3) has a band gap separating a valence band with $\mathcal{C}_- = 1$ from the conduction band. According to the bulk-boundary correspondence (2.2), this means that $n = 1$, in other words the Hall conductivity is e^2/h. The edge state that is responsible for this value can be visualized by solving for the band structure in a semi-infinite geometry. This means that we impose periodic boundary conditions on two opposite edges, while imposing open boundary conditions on the other two edges. The wavenumber in only one of the two directions is then a good quantum number (e.g., k_x) and in general we then obtain pictures as schematically shown in Figure 2.2. Clearly, a gapless mode can then be seen. Moreover, n is then related to the number of crossings of the edge states with the Fermi energy. We can define this more precisely by saying that a crossing with positive slope gives a positive contribution, while a negative slope gives a negative contribution.

With this picture and the concept of adiabatic connectivity, we can also see the occurrence of protected edge currents more intuitively as follows. We can think of the material as being placed in a trivial vacuum that also has a band gap (namely, a gap for positrons and electrons in the Dirac picture). The two-dimensional material can then be seen as infinitely many one-dimensional lines that continuously interpolate between a non-trivial vacuum and a trivial one, in the direction perpendicular to the edge. Because of adiabatic connectivity, such an interpolation can only occur if the band gap closes at the edge, which explains the occurrence of a gapless mode.

The above discussion can also be generalized to multi-band models. In particular, we can think of the circulating current phases by Varma that were introduced in Chapter 1. The various current patterns that are possible explicitly break time-reversal symmetry. An interesting question is then whether the Hamiltonian with the mean-field corrections from the interaction may give rise to QAH states. This question was answered by Sun and Fradkin [37]. They showed that if the model breaks inversion and time-reversal symmetry, but conserves the product, then the system cannot host a QAHE.
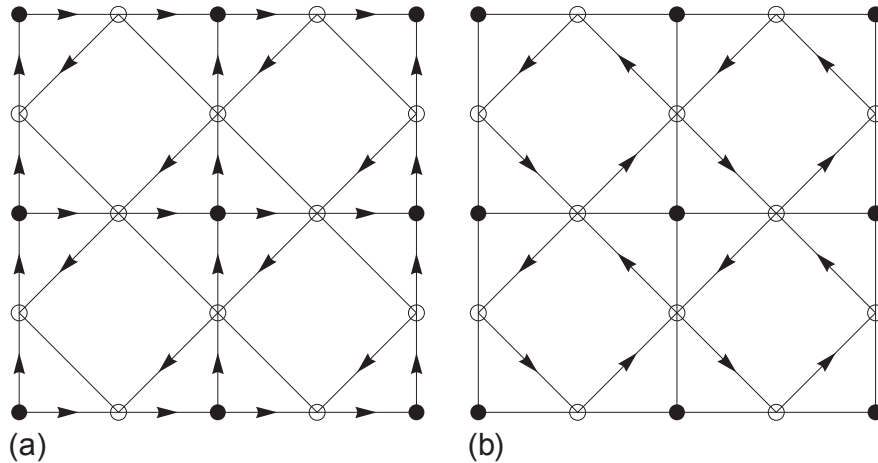
Figure 2.3: Two examples of Varma phases. The one shown in (a) breaks inversion and time-reversal but does conserve the product. For this reason it does not host a QAH response. However, the state in (b) does satisfy the correct requirements. Figure adapted from [37].

In this light, for the examples shown in Figure 2.3 only pattern (b) satifies this condition. Later, He, Moore and Varma related this to the occurrence of singularities in the wave function [38]. This example illustrates the fact that although time-reversal symmetry breaking is a necessary condition for the QAHE, it is certainly not a sufficient one.

2.3 Quantum spin Hall effect

All the QHEs in two dimensions need TRS breaking to occur. However, in 2005 a new type of topological quantum matter was proposed by Kane and Mele, the so-called quantum spin Hall effect (QSHE) [51, 52]. They proposed a time-reversal symmetric model of graphene, where spin-orbit coupling (SOC) plays an important role, such as a Rashba SOC and intrinsic SOC. If the Rashba term is zero, then spin is conserved and the Kane and Mele model is just like two copies of the Haldane model for each spin component. Although initially proposed for the honeycomb lattice, it seemed that the SOC in real graphene was too weak to host a QSHE. However, it did not take long until the QSHE was realized experimentally in HgTe/CdTe quantum wells [53] after the theoretical formulation by Bernevig, Hughes and Zhang [54].

Because the QSH insulator necessarily preserves time-reversal symmetry, it means that $n = 0$ for every Fermi energy. In other words, there is no quantum Hall conductivity. Instead, the QSHE is characterized by a non-vanishing spin Hall conductivity that is the result of a transverse spin current along the edges. Moreover, these edge states are topologically protected, which ensures that they are robust against impurities, in sharp contrast to the spin Hall effects that were known at that time.

However, there are some important differences. First of all, the spin currents are carried by helical edge states, instead of chiral ones, which means that the direction of motion is correlated with its spin. Because of the spin degree of freedom, we always have an even number of them, i.e. the helical
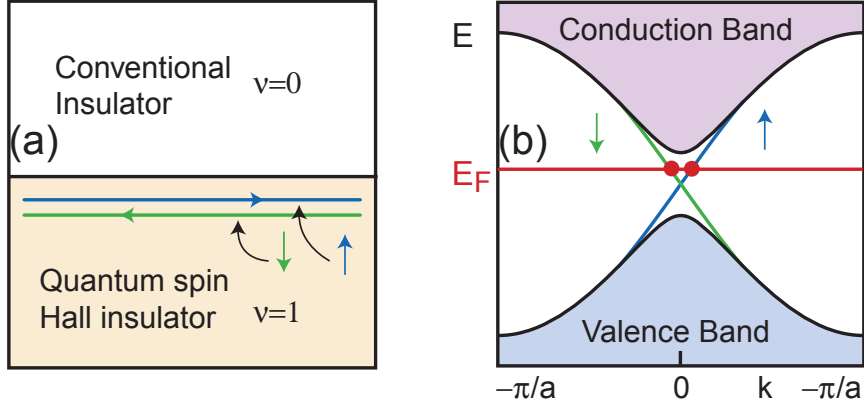
Figure 2.4: Schematic figure showing the QSHE. In (a) we observe the presence of a pair of helical edge state by connecting a non-trivial material with $\nu = 1$ with a trivial vacuum. These edge state can be visualized in the spectrum by solving for a semi-infinite geometry. Figure adapted from Ref. [41].

edge states come in pairs on a given edge. This is schematically shown in Figure 2.4. Secondly, this spin Hall conductivity is only quantized if spin is conserved. For instance, we can define a spin Hall conductivity by a difference of the expectation value of $\hat{S}_z$ for left (L) and right movers (R) at the Fermi energy

$$\sigma_{SH} = \frac{e}{h}(\langle \hat{S}_z \rangle_L - \langle \hat{S}_z \rangle_R)|_{E_F}. \tag{2.5}$$

If spin is not conserved, then the edge states are not necessarily eigenstates of $\hat{S}_z$. Finally, the QSHE is characterized by a so-called $\mathbb{Z}_2 := \mathbb{Z}/2\mathbb{Z}$ index ν instead of an integer $\mathbb{Z}$. In other words, the QSHE is characterized by an integer modulo 2, which we represent by either 0 or 1, which denote either the trivial or the non-trivial states, respectively. If $\nu = 0$, there is an even number of edge state pairs on a given edge, while for $\nu = 1$ we have an odd number. For this reason, the QSH insulator is maybe more accurately described as a $\mathbb{Z}_2$ topological insulator. The fact that an even number of edge state pairs is trivial, needs more explanation. The reason for this is that the time-reversal symmetry, that offers protection for these helical edge states, gives rise to non-trivial consequences.

To make this idea more transparent, let us consider a system of spin-$1/2$ particles on a lattice, described by a time-reversal symmetric Hamiltonian $\hat{H}$. It can then be shown that there exists an anti-unitary operator Θ, with $\Theta^2 = -\mathbb{1}$ (or $\Theta^2 = \mathbb{1}$ for integer spin particles), such that the Bloch Hamiltonian $\mathcal{H}(\mathbf{k})$ satisfies $\Theta\mathcal{H}(\mathbf{k})\Theta^{-1} = \mathcal{H}(-\mathbf{k})$. The operation Θ can be written as $\Theta = \mathcal{K}U$, where U is unitary and $\mathcal{K}$ is complex conjugation, the latter contribution explaining why it is anti-unitary. This condition on $\mathcal{H}(\mathbf{k})$ implies that for any state characterized by $(\mathbf{k}, \uparrow)$ there is a time-reversed partner $(-\mathbf{k}, \downarrow)$ with the same energy. However, at the time-reversal invariant momenta (TRIM) $\mathbf{\Gamma}$, defined by the condition $\mathbf{\Gamma} = -\mathbf{\Gamma} + \mathbf{G}$, with $\mathbf{G}$ a reciprocal lattice vector, we have the additional property[1] that $[\mathcal{H}(\mathbf{\Gamma}), \Theta] = 0$. This implies that $\mathcal{H}(\mathbf{\Gamma})$ and Θ have the same basis of

---

[1] Notice that this property heavily relies on the fact that the Hamiltonian matrix has a BZ periodicity. However, in
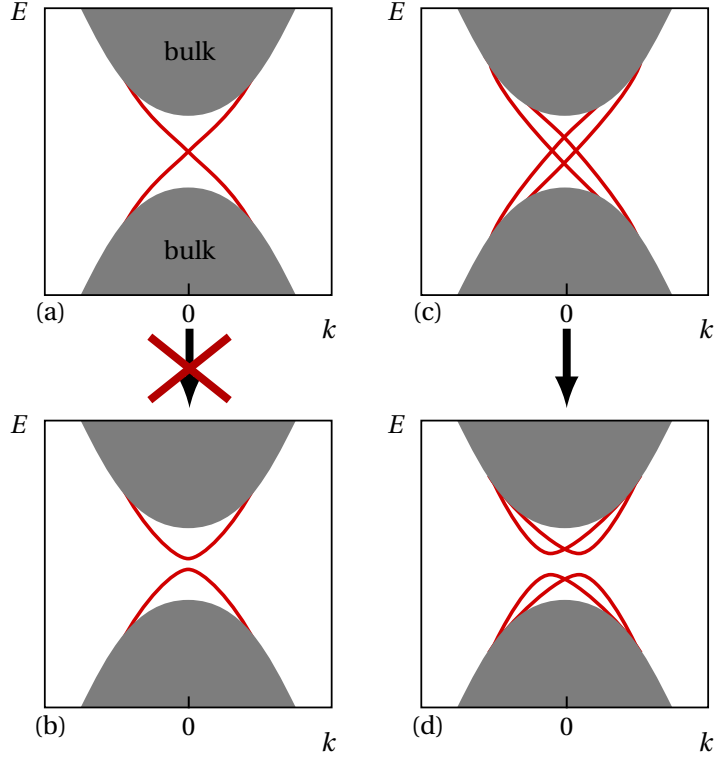
Figure 2.5: Example why the QSHE is characterized by a $\mathbb{Z}_2$ invariant. It is not possible to create a gap in the edge state spectrum for a single pair of helical edge states on a given edge. Such TRS perturbations always violate Kramers theorem (see (a)→(b)). However, this is possible with two pairs of edge states ((c)→(d)). Figure adapted from Ref. [57].

eigenvectors. Let us now consider such an eigenvector which we will denote by $|\chi\rangle$ with eigenvalue λ, that we assume to be non-degenerate. Applying Θ twice to such a state, we have that $\Theta^2|\chi\rangle = \Theta\lambda|\chi\rangle = \lambda^*\Theta|\chi\rangle = |\lambda|^2|\chi\rangle$, where the second equality comes from the fact that we have to pull λ through Θ that contains $\mathcal{K}$. However, $\Theta^2 = -\mathbb{1}$ and this contradicts the fact that λ is non-degenerate. This proves Kramers theorem [56], which in our formulation states that any eigenvalue evaluated at a TRIM is at least doubly degenerate.

Now the topological protection by TRS should be clear. An even number of edge state pairs can be pushed out of the band gap by a TRS perturbation, because such perturbations still satisfy Kramers theorem. This is in contrast to an odd number of edge state pairs, that could only be removed out the gap by a band gap closing, see also Figure 2.5.

---

multiband tight-binding models, this is not necessarily true. This is because it is a common convention in the literature and in this thesis to let the Fourier transform depend on the position of the lattice site within the unit cell. However, this is not a problem. Namely, such a Hamiltonian is always unitary equivalent to a matrix that is BZ periodic, with a unitary transformation given by a diagonal matrix that contains suitable phase factors. Alternatively, we can redefine the unitary part in Θ by such a matrix. For a more thorough discussion on the issue of BZ periodicity, see Ref. [55].

We finally note that the 2D $\mathbb{Z}_2$-TI has a generalization to 3D [58]. In contrast to the 2D case, it is characterized by four $\mathbb{Z}_2$ invariants. The material can then be classified as a weak TI, a system that consists of layers of 2D QSH states and are weak against disorder, or a strong TI, that is a genuinely new topological state for which the surface acts as a topological metal. Here, the Fermi surface encloses an odd number of Dirac cones.

2.4   Other types of topological quantum matter

From the above discussion, it is clear that TRS plays an important role for the QSHE to occur. However, there are other discrete symmetries that play also an important role in the classification of topological quantum matter. One is for example the so-called particle-hole symmetry. If the Hamiltonian is particle-hole symmetric (PHS), then there exists an anti-unitary operator Ξ with $\Xi^2 = \pm\mathbb{1}$ such that the Hamiltonian matrix satisfies $\Xi\mathcal{H}(\mathbf{k})\Xi^{-1} = -\mathcal{H}(-\mathbf{k})$. Such a condition implies that for every state $\mathbf{k}$ with energy E, there is a state $-\mathbf{k}$ with energy $-E$. Examples of such systems are superconductors, for which the Bogoliubov-de Gennes Hamiltonian is PHS by construction. This opens the possibility to have topological superconductors, for which the PHS implies the possible existence of gapless Majorana modes. The final discrete symmetry is the so-called chiral symmetry (or sublattice symmetry), which is a combination of time-reversal and particle-hole transformations. It is represented by a unitary operator Π, and a Hamiltonian matrix with this symmetry satisfies $\Pi\mathcal{H}(\mathbf{k})\Pi^{-1} = \mathcal{H}(-\mathbf{k})$.

According to these symmetries, topological states of matter can be classified in a systematic way [59, 60]. This defines the so-called ten-fold way, for which ten symmetry classes are found. For each such class, this classification shows whether a topological invariant can be found for a given dimension. The result is shown in Table 2.1 for $d = 1, 2, 3$, which are the only dimensions that are relevant for us.

From this table, we see that in each dimension five types of topological quantum matter can be found, that can either be classified by a $\mathbb{Z}$ or a $\mathbb{Z}_2$ invariant. The IQHE/QAHE discussed previously falls into the A class for $d = 2$, while the $\mathbb{Z}_2$ topological insulators of the previous section for $d = 2, 3$ are classified as AIII. Some entries represent topological superconductors, such as the CI class in three dimensions. This TRI singlet superconductor can be characterized according to a winding number that takes on even values only [61]. The non-trivial phase is characterized by an even number of linearly dispersing surface Andreev states. These bound states give a linear contribution to the surface density of states, and these can be detected with STM. As another example, we have the DIII class for $d = 3$, the so-called non-centrosymmetric superconductors. Here the fully gapped phases are characterized by a winding number, while nodal superconducting phases are characterized by a topological charge [62]. Also the B-phase of the fermionic superfluid He-3 falls into this class [63].

However, this classification only works for Hamiltonians with single-particle like terms. The real influence of interactions is still not entirely clear. Moreover, there are also proposals to extend the classification as defined above by taking into account the underlying lattice structure. Juričić et al. [64] showed that a dislocation inserted into the lattice structure can bind zero modes similar to a π-flux, depending on where the band gap opens in the 1BZ.

Table 2.1: Tenfold way classification of topological invariants according to dimension (up to $d = 3$) and the operators Θ, Ξ and Π. A zero means that this symmetry is absent, while a presence of such a symmetry is specified by ± 1. Here the sign depends on the type of particles that we consider and thus on whether the relevant operator squares to plus or minus the identity.

Class	Θ	Ξ	Π	$d = 1$	$d = 2$	$d = 3$
A	0	0	0	0	$\mathbb{Z}$	0
AIII	0	0	1	$\mathbb{Z}$	0	$\mathbb{Z}$
AI	1	0	0	0	0	0
BDI	1	1	1	$\mathbb{Z}$	0	0
D	0	1	0	$\mathbb{Z}_2$	$\mathbb{Z}$	0
DIII	-1	1	1	$\mathbb{Z}_2$	$\mathbb{Z}_2$	$\mathbb{Z}$
AII	-1	0	0	0	$\mathbb{Z}_2$	$\mathbb{Z}_2$
CII	-1	-1	1	$\mathbb{Z}$	0	$\mathbb{Z}_2$
C	0	-1	0	0	$\mathbb{Z}$	0
CI	1	-1	1	0	0	$\mathbb{Z}$

2.5 Optical lattices as a tool to study topological quantum matter

One of the central themes in this thesis is the investigation of the QSHE on the Lieb lattice. One of the most appealing experimental set-ups where we can realize this are the so-called optical lattices. We will only sketch the main ideas and refer to many of the excellent reviews for this subject (e.g., see ref. [65]). This is because we will not use the optical lattice idea anywhere explicitly in this thesis.

Let us now roughly sketch the principle behind optical lattices. By using a suitable laser set-up, a standing wave pattern of laser intensities can be realized. When loaded with cold atoms (fermions or bosons), this pattern acts as a periodic potential in which the atoms can move by virtue of the AC Stark effect. Such a potential also occurs in real electron systems, where it is provided by the ionic background. There are however differences, such as the fact that atoms are neutral, instead of charged, like the electrons. Secondly, the scales are different. The typical lattice constant in real materials is on the order of Å, while in optical lattices it is determined by the wavelength of the lasers λ, which can be of the order 500 nm. Optical lattices have the advantage over real materials that they are free of impurities. More importantly, they provide the possibility to tune the interaction strength and kinetic energy of the atoms to a very high accuracy by simply changing the laser intensities. This latter property makes optical lattices especially suitable to study various model systems in condensed matter physics to a very high degree of precision. For example, the Mott insulator-superfluid transition that was predicted for the Bose-Hubbard model [66, 67] has indeed been experimentally observed with the help of these cold atom systems [68].

There are various proposals to realize the Lieb lattice with cold atoms [69, 70]. By the laser
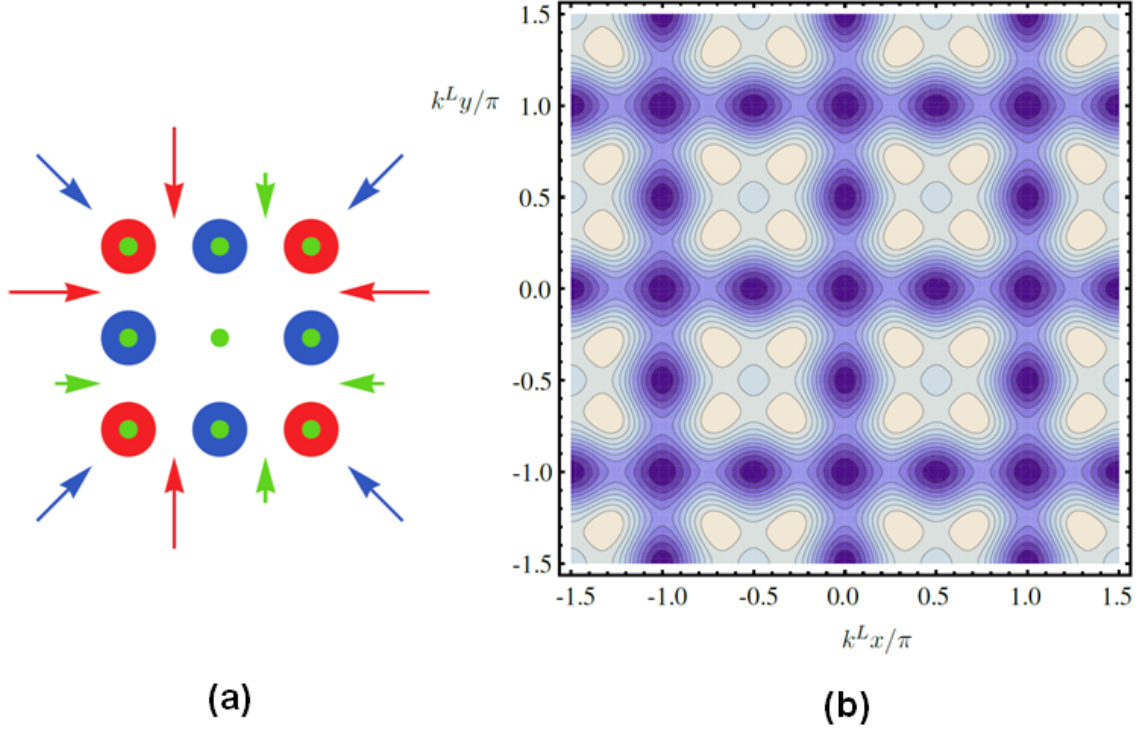
Figure 2.6: (a) Laser set-up for generating the Lieb lattice as an optical lattice. Picture adapted from [69]. (b) The optical potential that this laser arrangement produces.

arrangement shown in Figure 2.6(a), an optical potential landscape as given by

$$
\begin{aligned}
V(x,y) =& V_1(\sin^2 k^L x + \sin^2 k^L y + \sin^2 2k^L x + \sin^2 2k^L y) \\
& + V_2 \left\{ \sin^2 \left[k^L(x+y) + \frac{\pi}{2} \right] + \sin^2 \left[k^L(x-y) + \frac{\pi}{2} \right] \right\}
\end{aligned}
\tag{2.6}
$$

can indeed be generated to provide the precise lattice geometry of the Lieb lattice. This is plotted in Figure 2.6(b). Having such a realization in mind, we can systematically investigate tight-binding models for this geometry. Normally, these models are only formally true in the limit of a strong periodic potential. However, with the help of cold atoms we can simulate them to a very high degree of accuracy. In the next chapter, we will consider such models that include for example a next-nearest-neighbour hopping parameter t'. We are especially interested in t' as being a tunable parameter, however we can already see from Figure 2.6 that such a parameter would always be much smaller than the nearest-neighbour hopping t. However, recently it has been shown that by shaking the optical lattice, the ratio t'/t can be tuned to in principle any possible value. This is performed by adding a periodic modulation to the Hamiltonian, which depends on a shaking frequency ω. This perturbation can be treated within Floquet theory [71] in the limit of $\hbar\omega \gg V_0$, with V_0 a typical lattice depth. We then find that the nearest-neighbour hopping parameter is renormalized by a Bessel function [72], while t' can be renormalized by a Bessel function with a different argument [73]. Indeed, this allows

one to tune t'/t, and it will be of importance later. Namely, we will see in the next chapter that tuning t' can lead to many interesting topological phase transitions on the Lieb lattice.

Finally, we remark that optical lattices also provide a versatile tool to detect edge states. However, this is not straightforward because there are no charge currents, but mass currents. Moreover, we have to be able to define sharp edges in the experiment. There are various proposals to realize and detect these edge states experimentally, for example by using angular-momentum sensitive Bragg spectroscopy by employing Raman transitions in an appropriate way [74]. Furthermore, the notion of sharp edges is not always necessary to observe the edge states, because it can be shown that topological invariants are still well-defined in a system with soft edges [75].

Chapter 3

Driving topological phase transitions with next-nearest neighbour hopping

In this chapter we will investigate various topological phase transitions on the Lieb lattice. The lattice geometry of such a two-dimensional square lattice with three sites per unit cell is shown in Figure 3.1, together with the first Brillouin zone (1BZ). Our focus here lies on tight binding (TB) models, where we assume that all particles loaded onto this lattice are in their respective ground states. For instance, when only nearest neighbour (NN) hopping is included in such a model, there are three (spin degenerate) bands, where two dispersing bands touch the flat middle band via a cone like dispersion at the M-point. There are various ways of separating the three bands from each other, for example by adding a dimerization term that staggers the hopping along the x- and y-direction or by including a Rashba spin orbit coupling (SOC) term. The resulting gaps are however topologically trivial, as was discussed by Weeks and Franz [39]. Nevertheless, they showed that an intrinsic SOC is able to separate the three bands by a topologically non-trivial band gap. Here, we will extend their work by also including next-nearest neighbour (NNN) hopping into their model. As we shall see next, this will give rise to new interesting topological phase transitions, not studied before. Some of the results in this chapter have been recently submitted for publication [76].

3.1 Tight binding Hamiltonian

Motivated by the above discussion, we will investigate the following tight binding model on a Lieb lattice,

$$\hat{H} = -t \sum_{\langle i,j \rangle;\sigma} \hat{s}_{i,\sigma}^\dagger \hat{s}_{j,\sigma} - t' \sum_{\langle\langle i,j \rangle\rangle;\sigma} \hat{s}_{i,\sigma}^\dagger \hat{s}_{j,\sigma} + i\lambda_{\text{ISO}} \sum_{\langle\langle i,j \rangle\rangle;\sigma,\sigma'} \hat{s}_{i,\sigma}^\dagger (\mathbf{e}_{ij} \cdot \boldsymbol{\sigma}_{\sigma\sigma'}) \hat{s}_{j,\sigma'}. \tag{3.1}$$

The first (second) term describes the (N)NN hopping process of a fermion with spin projection σ from a site i to a site j. Effectively, this model can be seen as fermions hopping between s-orbitals, hence we denote their respective creation (annihilation) operator by $\hat{s}_{i,\sigma}^\dagger$ ($\hat{s}_{i,\sigma}$). The final term describes an intrinsic SOC term with coupling constant λ_{ISO}. On a lattice, it has the form of a spin dependent NNN
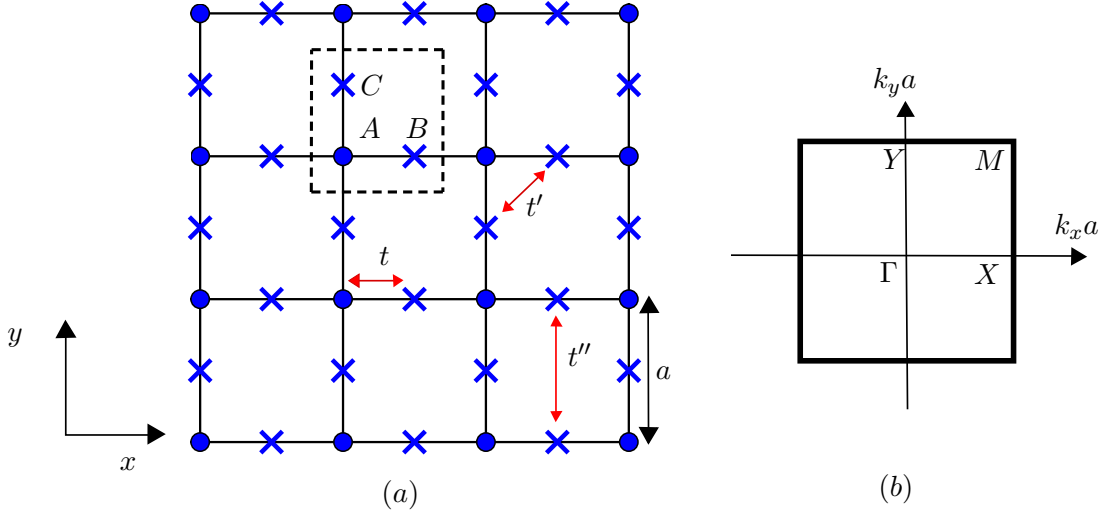
Figure 3.1: (a) The geometry of the Lieb lattice. The square unit cell with lattice constant a is indicated, together with the three sublattices (A, B, C). An example of a (N)NN hopping process t (t') is indicated by the red arrows. The third-nearest-neighbour hopping t'' is also indicated. The effect of this parameter will be investigated in Chapter 4. (b) First Brillouin zone of the Lieb lattice. The high symmetry points Γ, X, Y, and M are given.

hopping term. To describe this, we have defined a unit vector $\mathbf{e}_{ij} := (\mathbf{d}_{ik} \times \mathbf{d}_{kj})/|\mathbf{d}_{ik} \times \mathbf{d}_{kj}|$ in terms of the bond vectors $\mathbf{d}_{ik}$ and $\mathbf{d}_{kj}$ that connects the sites i and j via the unique intermediate site k. In this lattice geometry these bond vectors can be either $\pm a/2\mathbf{e}_x$ or $\pm a/2\mathbf{e}_y$ respectively, with a being the lattice constant. Finally, $\boldsymbol{\sigma} := (\sigma_x, \sigma_y, \sigma_z)$ is a vector of Pauli matrices.

In momentum space, the Hamiltonian can be written as

$$\hat{H} = \sum_{\mathbf{k} \in 1\mathrm{BZ}} \hat{\Psi}_{\mathbf{k}}^{\dagger} \mathcal{H}_{\mathbf{k}} \hat{\Psi}_{\mathbf{k}}, \quad \mathcal{H}_{\mathbf{k}} := \mathcal{H}_{\mathbf{k}}^0 \otimes \mathbb{1}_{2\times 2} + i\mathcal{H}_{\mathbf{k}}^{\mathrm{ISO}} \otimes \sigma_z, \tag{3.2}$$

in the basis $\hat{\Psi}_{\mathbf{k}} := (\hat{\Psi}_{\mathbf{k},\uparrow}, \hat{\Psi}_{\mathbf{k},\downarrow})$, where $\hat{\Psi}_{\mathbf{k},\sigma} := (\hat{s}_{A,\mathbf{k},\sigma}, \hat{s}_{B,\mathbf{k},\sigma}, \hat{s}_{C,\mathbf{k},\sigma})$. The 3×3 real matrices $\mathcal{H}_{\mathbf{k}}^0$ and $\mathcal{H}_{\mathbf{k}}^{\mathrm{ISO}}$ are given by

$$\mathcal{H}_{\mathbf{k}}^0 = \begin{pmatrix} 0 & -2t\cos(k_x a/2) & -2t\cos(k_y a/2) \\ -2t\cos(k_x a/2) & 0 & -4t'\cos(k_x a/2)\cos(k_y a/2) \\ -2t\cos(k_y a/2) & -4t'\cos(k_x a/2)\cos(k_y a/2) & 0 \end{pmatrix} \tag{3.3}$$

and

$$\mathcal{H}_{\mathbf{k}}^{\mathrm{ISO}} = 4\lambda_{\mathrm{ISO}} \begin{pmatrix} 0 & 0 & 0 \\ 0 & 0 & -\sin(k_x a/2)\sin(k_y a/2) \\ 0 & \sin(k_x a/2)\sin(k_y a/2) & 0 \end{pmatrix}. \tag{3.4}$$

It turns out that $\mathcal{H}_{\mathbf{k}}$ is block diagonal of the form $\mathrm{diag}(\mathcal{H}_{\mathbf{k}}^0 + i\mathcal{H}_{\mathbf{k}}^{\mathrm{ISO}}, \mathcal{H}_{\mathbf{k}}^0 - i\mathcal{H}_{\mathbf{k}}^{\mathrm{ISO}}) =: \mathrm{diag}(\mathcal{H}_{\mathbf{k}}^{\uparrow}, \mathcal{H}_{\mathbf{k}}^{\downarrow})$. This means that the blocks corresponding to the spin-up and spin-down projections are related by
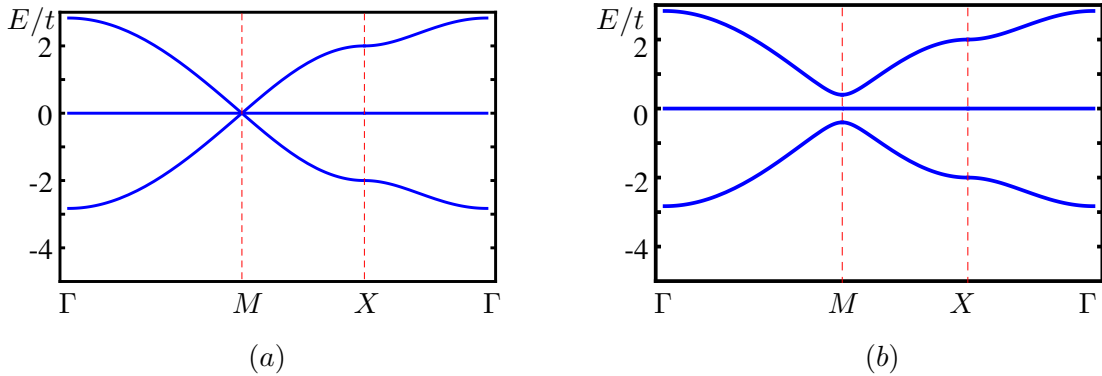
Figure 3.2: Gap opening at the M-point for $\lambda_{\text{ISO}} \neq 0$ and $t' = 0$. (a) The upper and lower bands touch the middle flat band at the M-point, while a gap appears if the intrinsic SOC is turned on, as shown in (b).

complex conjugation, $\mathcal{H}_{\mathbf{k}}^{\uparrow} = (\mathcal{H}_{\mathbf{k}}^{\downarrow})^*$. Moreover, these blocks are Hermitian, giving the well-known result that this particular form of intrinsic SOC cannot lift the spin degeneracy. For calculating the energy spectrum, it thus suffices to restrict our attention to one spin component, while keeping in mind that the resulting bands are doubly degenerate. Notice that the above model describes fermions on the Lieb lattice with complex NNN hopping, where the imaginary part stems from the intrinsic SOC.

3.2 Imaginary NNN hopping

Let us first consider the case where $t' = 0$. The resulting dispersion relations can be found in Figure 3.2 for $\lambda_{\text{ISO}} = 0$ and $\lambda_{\text{ISO}} \neq 0$ respectively. In the first case, we see that there is a single cone like dispersion touching a flat band at the M-point. It is remarkable that there is only one such cone in the 1BZ, because one would naively say that that there should always be an even number of Dirac cones by the fermion doubling theorem of Nielsen and Ninomiya [77]. However, the presence of the flat band gives a possibility to circumvent this theorem [78], because the low-energy Hamiltonian can only be expressed in matrices that form a representation of $\mathfrak{su}(2)$, but these do not form a Clifford algebra. Examples of these type of touchings are not unique for the Lieb lattice, since they can also be found in for example the kagome lattice with a staggered flux [79].

The effect of λ_{ISO} is to open a gap at the M-point as is seen in Figure 3.2(b). This is actually the case studied by Weeks and Franz [39]. They showed that the system is characterized by a non-trivial $\mathbb{Z}_2$ invariant ν, which can be calculated rather easily from the parity eigenvalues at the TRIM, because the system respects inversion symmetry [58]. However, we will show that both gaps can exhibit a QSHE in a different way, by using the fact that spin is conserved, since the SOC term is only proportional to σ_z. This means that this model can be seen as two independent copies of the spin-up and spin-down, making the Chern number a well-defined quantity for a single spin projection. The advantage of investigating the Chern numbers instead of ν is that it is directly related to the spin Hall conductivity.

Without loss of generality, let us focus on the spin up component and assume $\lambda_{\text{ISO}} > 0$. The

Hamiltonian can then be written as $\mathcal{H}_{\mathbf{k}}^{\uparrow} := \mathbf{R}\cdot\mathbf{L}$, where $\mathbf{R} = (R_1, R_2, R_3)$ with $R_1 = -2t\cos(k_x a/2)$, $R_2 = -2t\cos(k_y a/2)$ and $R_3 = 4\lambda_{\mathrm{ISO}}\sin(k_x a/2)\sin(k_y a/2)$. Furthermore, $\mathbf{L} := (L_1, L_2, L_3)$ is a vector of the following Gell-mann matrices

$$L_1 = \begin{pmatrix} 0 & 1 & 0 \\ 1 & 0 & 0 \\ 0 & 0 & 0 \end{pmatrix}, \quad L_2 = \begin{pmatrix} 0 & 0 & 1 \\ 0 & 0 & 0 \\ 1 & 0 & 0 \end{pmatrix}, \quad L_3 = \begin{pmatrix} 0 & 0 & 0 \\ 0 & 0 & -i \\ 0 & i & 0 \end{pmatrix}. \tag{3.5}$$

This set of matrices satisfy the commutation relations $[L_i, L_j] = i\epsilon_{ijk}L_k$, so they form a basis for the spin-1 representation of the Lie algebra $\mathfrak{su}(2)$. Because of this particular structure of the Hamiltonian, it is possible to calculate the Chern numbers analytically, since here they have a simple interpretation as a winding number. This was demonstrated by He, Varma and Moore [38], and we will apply their method below. In the following, we set the lattice constant $a = 1$.

The eigenvalues of $\mathcal{H}_{\mathbf{k}}^{\uparrow}$ are found to be $\epsilon_{\pm} = \pm R$ and $\epsilon_0 = 0$ with $R := |\mathbf{R}|$. Observe that there is a full gap between the energy bands for $R_3 \neq 0$ (Figure 3.2), making the Chern number a well-defined quantity. The eigenstates are also readily obtained by employing for instance a method using vector products (see the Appendix A). Because of the 3×3 structure of the Hamiltonian, there is some freedom for choosing the eigenstates, which are related by $U(1)$ gauge transformations. As He *et al.* [38] already pointed out, this gauge dependence does not show up in the Berry curvature and hence the Chern number is independent of a particular choice of eigenstates. Abbreviating an eigenstate as $|\Omega\rangle = (\alpha, \beta, \gamma) := \prod_{\mathbf{k},\sigma}(\alpha\hat{s}_{A,\mathbf{k},\sigma}^{\dagger} + \beta\hat{s}_{B,\mathbf{k},\sigma}^{\dagger} + \gamma\hat{s}_{C,\mathbf{k},\sigma}^{\dagger})|0\rangle$, where it is understood that $\mathbf{k}$ is restricted to the 1BZ, we find the eigenstates

$$|\Omega_{\pm}\rangle = \frac{1}{\sqrt{2(R^2 - R_1^2)}R}(\pm RR_2 + iR_1 R_3, R_1 R_2 \pm iRR_3, R^2 - R_1^2), \tag{3.6}$$

$$|\Omega_0\rangle = \frac{1}{R}(iR_3, R_2, -R_1). \tag{3.7}$$

In the thermodynamic limit, $\mathbf{k}$ becomes a continuous variable which allows us to take derivatives with respect to the wave numbers k_x and k_y. The Berry connections corresponding to the above states then read

$$A_{\mu}^{\pm} := -i\langle\Omega_{\pm}|\partial_{\mu}|\Omega_{\pm}\rangle = \frac{\mp R_1}{R(R^2 - R_1^2)}(R_3\partial_{\mu}R_2 - R_2\partial_{\mu}R_3), \tag{3.8}$$

$$A_{\mu}^{0} := -i\langle\Omega_0|\partial_{\mu}|\Omega_0\rangle = 0, \tag{3.9}$$

where we have abbreviated $\partial_{\mu} := \partial/\partial k_{\mu}$ for $\mu = x, y$. Clearly the Chern number for the band ϵ_0 is zero, so we will focus only on the bands $\epsilon_{\pm}$. The Berry curvature for these bands is given by

$$F_{xy}^{\pm} = \partial_x A_y^{\pm} - \partial_y A_x^{\pm} = \mp\hat{\mathbf{R}} \cdot (\partial_x\hat{\mathbf{R}} \times \partial_y\hat{\mathbf{R}}), \tag{3.10}$$

with $\hat{\mathbf{R}} := \mathbf{R}/R$. The Chern number is then given by

$$\mathcal{C}_{\pm}^{\uparrow} = \frac{1}{2\pi}\int_{1\mathrm{BZ}} d^2\mathbf{k}\, F_{xy}^{\pm} \tag{3.11}$$

$$= \mp\frac{1}{4\pi}\int_{-\pi}^{\pi} dk_x \int_{-\pi}^{\pi} dk_y \frac{t^2\lambda_{\mathrm{ISO}}(c_y^2 s_x^2 + c_x^2 s_y^2 + s_x^2 s_y^2)}{(t^2 c_x^2 + t^2 c_y^2 + 4\lambda_{\mathrm{ISO}} s_x^2 s_y^2)^{3/2}} = \mp 1, \tag{3.12}$$

32

with $s_\mu := \sin(k_\mu/2)$ and $c_\mu := \cos(k_\mu/2)$ for $\mu = x, y$. To summarize, we have for the spin up projection $\mathcal{C}^\uparrow := (\mathcal{C}_-^\uparrow, \mathcal{C}_0^\uparrow, \mathcal{C}_+^\uparrow) = (1, 0, -1)$. Obviously, for the spin down component, we have $\mathcal{C}^\downarrow = -\mathcal{C}^\uparrow$. We remark that from this result we immediately get the Chern numbers for $\lambda_{\mathrm{ISO}} < 0$ by interchanging the roles for spin up and spin down. Since the Hamiltonian is diagonal in spin space, we can define a spin Chern number [1] for the bands as $\mathcal{C}_{\mathrm{spin}} := \mathcal{C}^\uparrow - \mathcal{C}^\downarrow$. Notice that because of the symmetry between the spin components, we have that $\mathcal{C}_{\mathrm{spin}} = 2\mathcal{C}^\uparrow$. By virtue of the bulk-boundary correspondence, the spin Hall conductivity in units of the spin conductivity quantum [2] $e/4\pi$ then equals

$$\sigma_{\mathrm{SH}} := \sum_{\alpha:\, \epsilon_\alpha < \epsilon_F} \mathcal{C}_{\mathrm{spin},\alpha}, \tag{3.13}$$

where the summation is over the filled bands (i.e., ϵ_F is the Fermi energy) . Notice that σ_{SH} is necessarily quantized in these units because the edge modes are eigenstates of $\hat{S}_z$ with eigenvalue $\pm\hbar/2$. The $\mathbb{Z}_2$-index is then related to spin Hall conductivity by $\nu = \sigma_{SH}/2$ mod 2.

3.3 Real NNN hopping

Let us now consider the case where $t' \neq 0$, which can be seen as the real part of the NNN hopping term in the momentum space. We shall see that this contribution breaks particle-hole symmetry. This case is thus in a sense more complicated than the previous case, because the Hamiltonian matrix cannot be written in the form $\tilde{\mathbf{R}} \cdot \tilde{\mathbf{L}}$, with $\tilde{\mathbf{L}}$ a vector of matrices that form a basis for a Lie algebra that is is isomorphic to $\mathfrak{su}(2)$. However, it is still possible to extend the components of $\tilde{\mathbf{L}}$ to a basis of $\mathfrak{su}(3)$. This means that the Chern number does not have a simple interpretation as a winding number. Moreover, the expressions for the eigenvalues are more complicated, although one can still find them analytically. Defining $R_4 := -4t' \cos(k_x a/2) \cos(k_y a/2)$ and $R := \sqrt{\sum_{i=1}^4 R_i^2}$, we find that the dispersions satisfy

$$\epsilon_\alpha = \frac{2R}{\sqrt{3}} \cos\left[\frac{1}{3} \arccos\left(\frac{3\sqrt{3} R_1 R_2 R_4}{R^3}\right) + \gamma_\alpha\right], \tag{3.14}$$

where the angle γ_α parametrizes the three solutions as $\gamma_- = 2\pi/3$, $\gamma_0 = -2\pi/3$ and $\gamma_+ = 0$. These solutions have been obtained by using Cardano's solution for the roots of a cubic polynomial, given the fact that we have only real roots.

We will now focus on the qualitative behaviour of the dispersions as function of t' when we set $\lambda_{\mathrm{ISO}} = 0$ (Figure 3.3), meaning that we have purely real NNN hopping. This will help us to understand the full complex case later. Let us start with $t' = 0$, for which the middle band is flat, as was already discussed before (see Figure 3.3(a), dashed lines). For $t' > 0$, the middle band starts to develop a maximum at the Γ-point (see Figure 3.3(a), continuous lines), and ultimately, this maximum touches the upper band for $t'/t = 0.5$ (Figure 3.3(b)). For $t'/t > 0.5$, tilted anisotropic Dirac cone like

---

[1] In the presence of spin mixing perturbations the collection of Chern numbers for the various bands can be seen as a matrix in spin space, meaning that it is not useful to define a spin Chern number. See also Ref. [80].

[2] There are various conventions for the units. If one thinks of a spin current as a difference of two charge currents, then σ_{SH} can be expressed in units of e^2/h. As a true spin current, it is in units of $\pm e/4\pi$, where the sign also depends on convention.
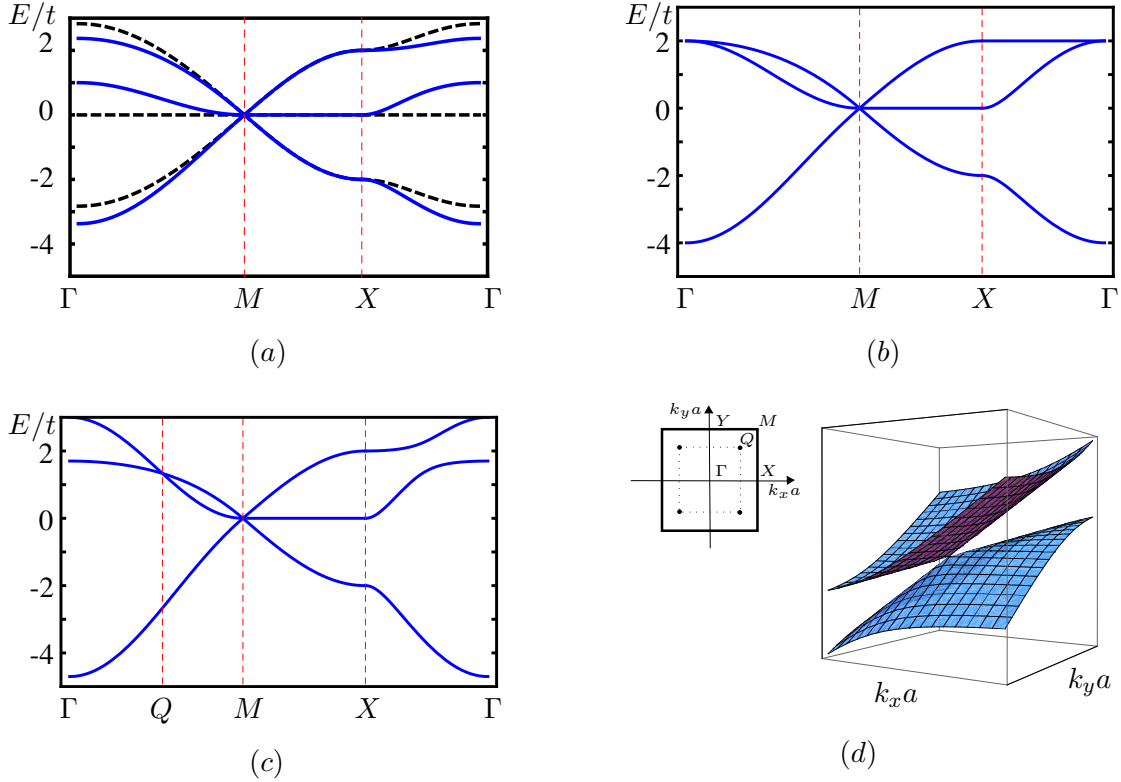
Figure 3.3: Dispersions for various values of t' along the high symmetry lines in the 1BZ. (a) The case where $t' = 0$ is shown by the black dashed line. For $0 < t' < 0.5t$ the middle band starts to develop a maximum at the Γ-point. This is shown in blue. (b) For $t' = 0.5$ the maximum at the Γ-point touches the upper band. (c) When $t' > 0.5t$ a tilted anisotropic Dirac cone forms at the Q-point. The Q-point is defined in (d), where also a three-dimensional picture of the anisotropic tilted Dirac cone at this point is shown. Finally, the four corners of the dotted square indicate the positions of the four tilted anisotropic Dirac cones in the 1BZ.

touchings occur at four inequivalent points in the 1BZ of the form $(\pm q, \pm q)$, where q is given by the condition $\cos(qa/2) = t/2t'$ for $t' > 0$ (see Figure 3.3(c)-(d)). Notice that these four solutions reflect the C_4 symmetry of the underlying lattice and that they do not coincide with high symmetry points in the 1BZ. Moreover, observe that the position of these cones in the 1BZ is tunable by t'. Finally, the result for $t' < 0$ can be obtained by changing E to $-E$ for every $\mathbf{k}$.

Next, we will show that the effective Hamiltonian around these points is a generalized Weyl Hamiltonian, meaning that the low energy structure of the dispersion is indeed that of a tilted anisotropic Dirac cone. Without loss of generality, we only consider the case $q > 0$ and set $\mathbf{k}_Q := (q, q)$. This means that we focus on the tilted Dirac cone at the Q-point defined in Figure 3.3(d). Taylor expanding,

we find for $i = x, y$

$$\cos(k_i a/2) = \cos(qa/2) - \frac{1}{2}\sin(q/2)(p_i a) - \frac{1}{8}\cos(q/2)(p_i a)^2 \tag{3.15}$$

$$= \frac{t}{2t'} - \frac{1}{2}\sqrt{1 - (t/2t')^2}(p_i a) - \frac{1}{8}t/2t'(p_i a)^2, \tag{3.16}$$

where we used that $\sin(\arccos x) = \sqrt{1 - x^2}$ and defined $\mathbf{k} := \mathbf{k}_Q + \mathbf{p}$. We use this to expand (3.3) entrywise to first order as $\mathcal{H}^0(\mathbf{k}) \simeq \mathcal{H}^0(\mathbf{k}_Q) + \delta\mathcal{H}(\mathbf{p})$. Then, we have that

$$\mathcal{H}^0(\mathbf{k}_Q) = -\frac{t^2}{t'}\begin{pmatrix} 0 & 1 & 1 \\ 1 & 0 & 1 \\ 1 & 1 & 0 \end{pmatrix}, \tag{3.17}$$

which has eigenvalues $\epsilon_1^0 = \epsilon_2^0 = t^2/t'$ and $\epsilon_3^0 = -2t^2/t'$, while the normalized eigenvectors are $|\psi_1\rangle = (-1, 0, 1)/\sqrt{2}$, $|\psi_2\rangle = (1, -2, 1)/\sqrt{6}$ and $|\psi_3\rangle = (1, 1, 1)/\sqrt{2}$. Notice that it is essential that the eigenvectors $|\psi_1\rangle$ and $|\psi_2\rangle$ that span the two-dimensional eigenspace corresponding to $\epsilon_1^0 = \epsilon_2^0$ are orthonormal. This can be achieved by using the Gram-Schmidt procedure. The first order correction to the Hamiltonian matrix is given by

$$\delta\mathcal{H}(\mathbf{p}) = t\sqrt{1 - \frac{t^2}{4t'^2}}\begin{pmatrix} 0 & p_x & p_y \\ p_x & 0 & p_x + p_y \\ p_y & p_x + p_y & 0 \end{pmatrix}. \tag{3.18}$$

Using the Luttinger-Kohn representation at the point $\mathbf{k}_Q$ [81], the matrix elements of the effective Hamiltonian $\mathcal{H}^{\text{eff}}$ read to first order in p_x and p_y

$$\mathcal{H}^{\text{eff}}_{\nu,\nu'} = \epsilon_\nu^0 \delta_{\nu,\nu'} + \langle\psi_\nu|\delta\mathcal{H}(\mathbf{p})|\psi_{\nu'}\rangle \tag{3.19}$$

with $\nu, \nu' = 1, 2$. We neglect the first term, which is equivalent to setting the zero of energy equal to the value at the band touching point $\mathbf{k}_Q$. The result is

$$\mathcal{H}_{\text{eff}}(\mathbf{p}) = -t\sqrt{1 - \frac{t^2}{4t'^2}}\begin{pmatrix} p_y & p_y/\sqrt{3} \\ p_y/\sqrt{3} & (4p_x + p_y)/3 \end{pmatrix}. \tag{3.20}$$

The above can be written as a generalized Weyl Hamiltonian

$$\mathcal{H}_{\text{eff}}(\mathbf{p}) = \sum_{\mu=0}^{3} \mathbf{v}_\mu \cdot \mathbf{p}\,\sigma_\mu, \tag{3.21}$$

where $\sigma_0 := \mathbb{1}_2$ and $\boldsymbol{\sigma} := (\sigma_1, \sigma_2, \sigma_3) = (\sigma_x, \sigma_y, \sigma_z)$ is a vector of Pauli matrices. We find

$$\mathbf{v}_0 = -\frac{t}{3}\sqrt{1 - \frac{t^2}{4t'^2}}\,(-2\mathbf{e}_x + \mathbf{e}_y), \tag{3.22}$$

$$\mathbf{v}_1 = -t\sqrt{\frac{1}{3}\left(1 - \frac{t^2}{4t'^2}\right)}\,\mathbf{e}_y, \tag{3.23}$$

$$\mathbf{v}_2 = \mathbf{0}, \tag{3.24}$$

$$\mathbf{v}_3 = -\frac{2t}{3}\sqrt{1 - \frac{t^2}{4t'^2}}\,(\mathbf{e}_x + \mathbf{e}_y). \tag{3.25}$$
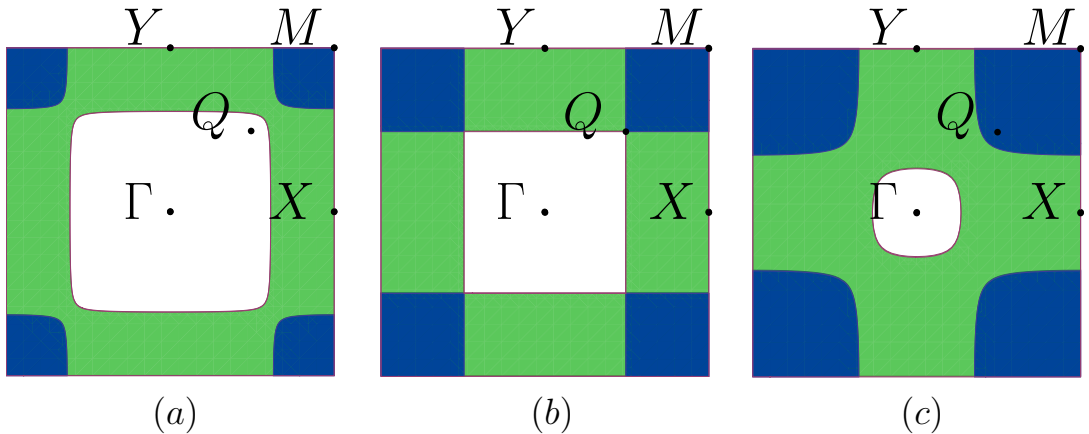
Figure 3.4: Fermi surfaces for $t' = 0.7t$, $\lambda_{\text{ISO}} = 0$ and chemical potential (a) below the Weyl points, (b) exactly at the Weyl points and (c) above the Weyl points. In green (blue) we denote the filled particle states from the middle (upper) band. For $t' = -0.7t$, the indicated regions would be filled hole states, with 'above' replaced by 'below' and vice versa.

In principle, one can transform the above Hamiltonian to a minimal Weyl Hamiltonian, as shown by Goerbig *et al.* [82]. For this, we first make a rotation in spin space to transform σ_z into σ_y. This is followed by a unitary transformation which is equivalent to a rotation in spin space around the σ_z axis, together with a rotation in momentum space. The rotation angles are then chosen in such way that the coefficient in front of σ_x is proportional to the momentum in the x-direction and similarly for the y-direction. In terms of the new parameters, one can then obtain a condition for which one can unambiguously assign the conduction and valence band for a Fermi energy around the band touching point. However, in our case we find that this maximum tilt condition is violated for all values of $t' > 0.5t$. Actually, this can also be seen by looking at the dispersions in Figure 3.3(d). As a consequence, the Fermi surfaces around the band touching point are open.

To demonstrate this behaviour, we have plotted the Fermi surfaces exactly at the Weyl points and slightly above/below it in Figure 3.4. These pictures reveal that exactly at the band touching point the Fermi surface is perfectly nested, while slightly above or below it, the nesting is imperfect. It would be interesting to add on-site interactions for these choices of chemical potential and investigate spin and charge density wave instabilities using the formalism proposed by Makogon *et al.* [83]. The fact that there is a multi-band Fermi surface may give rise to interesting effects. Moreover, extending this formalism to include longer-range interactions seem to be worthwhile.

The occurrence of open Fermi surfaces does not necessarily pose a problem for the application of the effective Hamiltonian in (3.21). However, as we shall see in the next section, the band that is projected out becomes topologically non-trivial for $\lambda_{\text{ISO}} \neq 0$, which hints to the fact that the generalized Weyl Hamiltonian does not properly take into account the topology of the system. One thus has to resort to the full tight binding Hamiltonian to get hold of these properties.
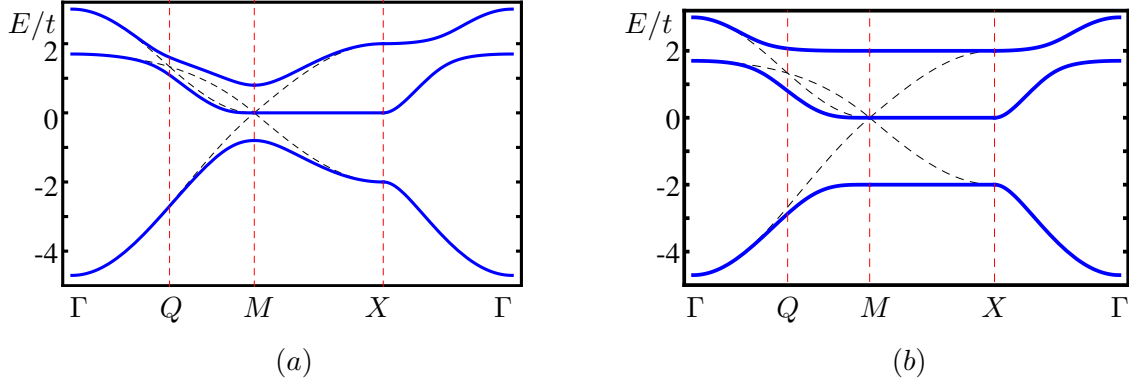
Figure 3.5: (a) The black dashed line indicates the dispersions for $\lambda_{\text{ISO}} = 0$ and the blue continuous line indicates the situation for $\lambda_{\text{ISO}} \neq 0$. There is no full gap when λ_{ISO} is below a critical value λ_{ISO}^c. (b) For a sufficiently large $\lambda_{\text{ISO}} > \lambda_{\text{ISO}}^c$, the spectrum is fully gapped.

3.4 Numerical evaluation of the Chern numbers for complex NNN hopping

Let us now consider the case $t' \neq 0$ and $\lambda_{\text{ISO}} \neq 0$. Regarding the topology of the bands, we already understand the case $t' < 0.5t$. Namely, such a state is adiabatically connected to the case for which $t' = 0$ and no band gap is closed in such a process. This means that the Chern numbers of the bands are exactly the same as if one would put $t' = 0$.

It is however more subtle for $t' > 0.5t$. As mentioned in the previous section a band touching point occurs at the Γ-point for $\lambda_{\text{ISO}} = 0$. Interestingly, this still occurs in the presence of intrinsic SOC, because $R_3 = 4\lambda_{\text{ISO}} \sin(k_x a/2) \sin(k_y a/2) = 0$ at the Γ-point for all values of λ_{ISO}. In a sense, the Γ-point is thus protected from the effects of the intrinsic SOC. Because the upper and middle band do touch when t' is increased above $0.5t$, the Chern numbers of the bands may change. For this reason it is worthwhile to be able to calculate the Chern numbers in the presence of a non-zero t'. An analytical evaluation of the Chern numbers as in section 3.2 is in principle possible, but the expressions become tedious to deal with. For this reason, we will choose to compute the Chern numbers numerically by resorting to the method proposed by Fukui *et al.* [84]. The analytical results presented before have been used to check the validity of our numerical code.

Before we present the results from this calculation, we would like to point out another subtlety that occurs in the band structure of our TB model for a genuinely complex NNN hopping. It is clear that for $t' \neq 0.5t$ all three bands are separated from each other at each point in the 1BZ. However, there is a parameter regime for which there is no full gap between the upper and middle band, although the bands are separated (Figure 3.5(a)). In this case, if the minimum of the upper band lies below the maximum of the middle band, we say that the spectrum exhibits a negative indirect band gap. We observe that a critical λ_{ISO} is needed to obtain a full gap between the middle and upper band (Figure 3.5(b)). The condition for such a full gap to occur is $\epsilon_0(\mathbf{k}_\Gamma) < \epsilon_+(\mathbf{k}_M)$. Whenever, this condition is not satisfied, a 2/3-filled system will always have both the upper band and the middle band partially

filled, which would classify the bulk as a semi-metal. Because of these bulk states that are present at this filling, it may not be possible to detect the edge states. Moreover, by a result of Haldane [85], the partially filled bands will in general give a non-quantized contribution to the spin Hall conductivity.

Notice that for 1/3-filling this problem does not occur, which means that the edge states can be experimentally observed. By symmetry, we have the same effects for $t' < 0$, but with 1/3- and 2/3- filling interchanged and "upper gap" replaced by "lower gap". Given this information, we can draw a 'phase' diagram in the $(t', \lambda_{\mathrm{ISO}})$-plane, for which we indicate the regions with distinct Chern numbers for the bands. Moreover, we can find the regions when there is a full gap between the (lower) upper band and the middle band for (1/3-) 2/3-filling.

Let us comment on the phases which occur in such a diagram, as is shown in Figure 3.6. Without loss of generality, let us focus on the case that $t' > 0$. For 2/3-filling, one has a semi-metal at the blue region in Figure 3.6. Outside this blue region, one could classify the material as a QSH insulator whenever $\lambda_{\mathrm{ISO}} \neq 0$ and $t' \neq 0.5t$. The first requirement is necessary, because for $\lambda_{\mathrm{ISO}} = 0$ the three bands are not separated, resulting in a metallic state (Figure 3.3). Recall that if the second requirement is not satisfied, there is a band touching point at the Γ-point. Consequently, it is not possible to assign a Chern number to the middle and upper bands separately.

For 1/3-filling, all the regions enclosed by the red lines and the line $t' = 0$ are QSH insulators with σ_{SH} given by (3.13). Just like above we have for this filling fraction that the case $\lambda_{\mathrm{ISO}} = 0$ is an ordinary metal. Finally, for $t' = 0.5t$ and $\lambda_{\mathrm{ISO}} \neq 0$, the Fermi energy lies in a gap with a completely filled band with non-zero (spin) Chern number, hence classifying it as a QSH insulator. The above discussion also holds for $t' < 0$, but with 1/3 and 2/3 interchanged and the word 'blue' replaced by 'green'. Moreover, for $\mathcal{C}_0^\sigma = \pm 2$, we have that σ_{SH} switches sign when going from 1/3-filling to 2/3-filling. This does not occur when the middle band is topologically trivial. Finally, we note that the various changes in Chern numbers after a transition can be understood in terms of the type and number of band touchings that occur exactly at the transition.

3.5 Formal equivalence with Varma phase

We could now ask ourselves the question whether we can also see the topological phase transitions from the previous section in QAH systems, in addition to the QSH systems. Indeed, this is possible, and for this we will show that the Hamiltonian in Eq. (3.2) is formally equivalent to the Hamiltonian of the Varma phase shown in Figure 2.3(b). Let us thus have a closer look at this circulating current state. From Ref. [38] it is known that the Hamiltonian with mean-field corrections from the order parameter r is given by

$$\mathcal{H}_{\mathbf{k}}^{CC} = \begin{pmatrix} 0 & its_x & its_y \\ -its_x & 0 & t's_x s_y + irc_x c_y \\ -its_y & t's_x s_y + irc_x c_y & 0 \end{pmatrix}, \tag{3.26}$$

where we abbreviated $s_i := \sin(k_i a/2)$ and $c_i := \cos(k_i a/2)$ for $i = x, y$. It turns that the Hamiltonian (3.2) that we studied before is equivalent to this Hamiltonian for a particular choice
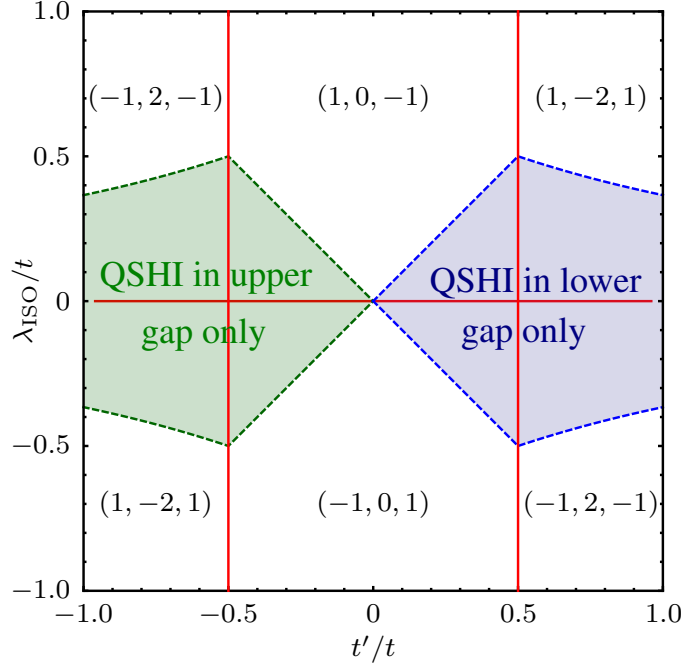
Figure 3.6: Phase diagram as function of λ_{ISO} and t'. The red lines indicate positions for which a band gap closes, meaning that the Chern numbers can change. In the regions enclosed by these red lines the various (spin) Chern numbers $\mathcal{C}^{\uparrow} = \mathcal{C}_{\text{spin}}/2$ are indicated. The blue (green) region indicates the parameter regime for which there is no full gap between the middle and upper (lower) band.

of spin component. To make this equivalence more precise, first shift the momentum in (3.26) by $\mathbf{k} \to \mathbf{k} + (\pi, \pi)$. Then perform a unitary transformation by using the matrix $U := \text{diag}(i, 1, 1)$. We find that $\mathcal{H}_{\mathbf{k}}^{\sigma} = U \mathcal{H}_{\mathbf{k}+(\pi,\pi)}^{CC} U^{\dagger}$ if we identify $t' \to -4t'$ and $r \to \pm 4\lambda_{\text{ISO}}$, where the plus (minus) sign refers to $\sigma = \downarrow$ ($\sigma = \uparrow$).

This formal equivalence is interesting because it means that this Varma phase can undergo the topological phase transitions studied in the previous section. This means that the phase diagram in Figure 3.6 could equally well apply to this Hamiltonian, with a suitable rescaling of the axes. The only difference is that it is not helical edge states that may reverse direction, but chiral ones because of explicit TRS breaking. Finally, these phase transitions were not discussed in Ref. [38], although they did mention the possibility that Chern numbers may change when bands start to touch.

3.6 Staggered hoppings

In Ref. [39] it was shown that a staggered NN hopping $t \pm \alpha$ along the x- and y-direction in the absence of SOC also opens a gap at the M-point. However, it was found that such a gap is topologically trivial. In light of Ref. [37] this is not surprising, because the Hamiltonian for a single spin projection conserves the product of time-reversal and inversion. Moreover, their Hamiltonian is formally

equivalent to a Varma phase that does not exhibit a QAHE.

However, despite of this, we still find it interesting to investigate such a contribution to the Hamiltonian, but with an intrinsic SOC present. Including the dimerization term, we find that the Hamiltonian changes to

$$\mathcal{H}_{\mathbf{k}} := \mathcal{H}_{\mathbf{k}}^0 \otimes \mathbb{1}_{2\times2} + i\mathcal{H}_{\mathbf{k}}^{\text{ISO}} \otimes \sigma_z + \mathcal{H}_{\mathbf{k}}^{\text{dim}} \otimes \mathbb{1}_{2\times2}, \tag{3.27}$$

with

$$\mathcal{H}_{\mathbf{k}}^{\text{dim}} = \begin{pmatrix} 0 & -2i\alpha s_x & -2i\alpha s_y \\ 2i\alpha s_x & 0 & 0 \\ 2i\alpha s_y & 0 & 0 \end{pmatrix}. \tag{3.28}$$

We could choose the relative signs in front of the sines differently, which corresponds to different dimerization patterns. However, this will not change the results that follow because it only amounts to a suitable transformation e.g., $(k_x, k_y) \rightarrow (k_x, -k_y)$ in momentum space. Let us now calculate the phase diagram for a fixed α by identifying the set of parameters for which a band touching occurs. However, this is in principle a difficult problem, because the dimerization α explicitly breaks the underlying C_4 symmetry of the lattice, but it can be solved numerically. Moreover, the condition for a negative indirect band gap was also calculated. The results are shown in Figure 3.7 for the staggered hopping contribution $\alpha = 0.3t$.
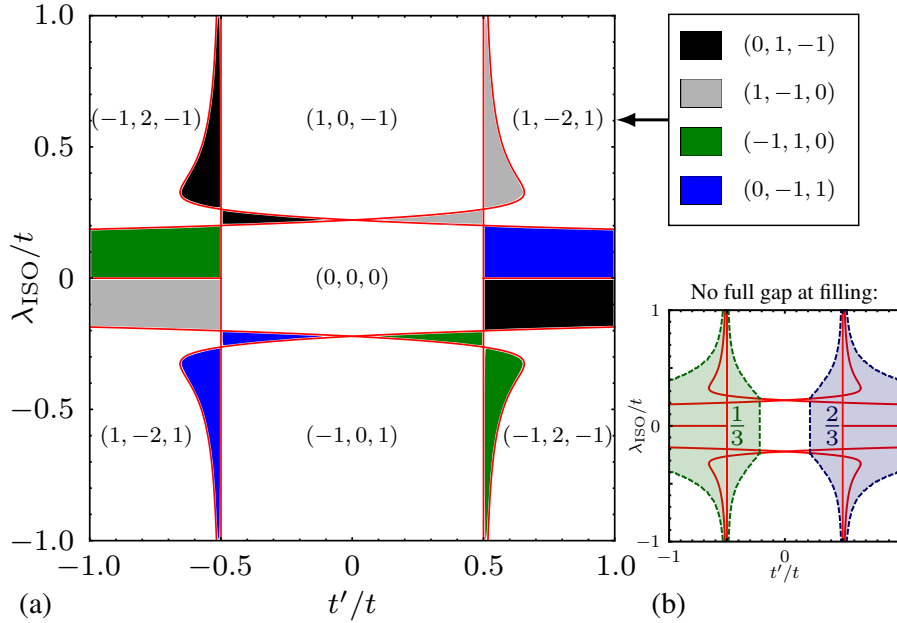
Figure 3.7: (a) Phase diagram as function of λ_{ISO} and t' for $\alpha = 0.3t$. This diagram should be read in the same way as the one in Figure 3.6. The combination of Chern numbers of the bands that do not occur in the $\alpha = 0$ case are indicated with colored regions. (b) A negative indirect band gap occurs in the green (blue) region, delimited by the dashed lines for $1/3$ $(2/3)$ filling.

There are a few qualitative differences compared to the case where $\alpha = 0$. First of all, we observe various new combinations of Chern numbers for the bands, which we indicate by the colored regions. These regions are larger if α is increased. For these regions, it can occur that the gaps are either trivial or host a QSHE with $\sigma_{SH} = \pm 2$. Finally, we see that the region for which a negative indirect band gap can occur is much larger. We observe for example that λ^c_{ISO} diverges near the transition line $|t'/t| = 0.5$. However, the additional features from the dimerization term are not washed out, because the indirect gap only occurs in one of the two gaps. Finally, we see that for $|t'| < |\alpha|/\sqrt{2}$ no negative indirect band gap can occur.

3.7 Some perspectives on other lattice geometries

The occurrence of these phase transitions driven by t' opens the question whether they can also occur in other lattices. Although other lattice geometries are not a focus of this thesis, we did investigate the kagome lattice, which has three sites per unit cel. Indeed, these phase transitions occur also in the kagome lattice. However, in the honeycomb lattice, with two sites per unit cell, they were only found at non-zero magnetic field. For this reason, we may conjecture that these type of topological phase transitions can only occur in multi-gap systems. The details of the relevant calculations, together with the results presented here have been recently submitted for publication [76].
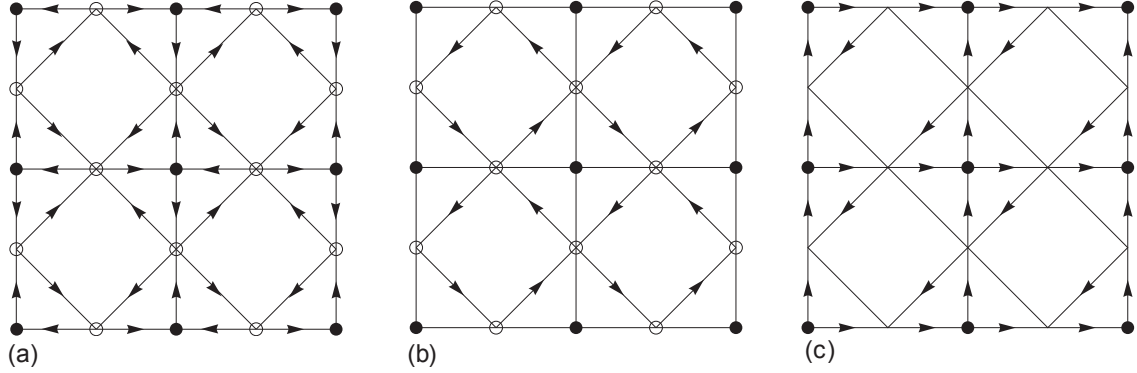
Chapter 4

Fermionic superfluidity

In this chapter, we will investigate fermionic superfluidity on the Lieb lattice at zero temperature in mean-field. Since our focus here will be on the weak coupling limit, it is important to first understand the band structure without any mean field corrections. There are several possible band structures from which we can start. One way is to begin with the model presented in the previous section with $\lambda_{\mathrm{ISO}} = 0$ and $t' > 0.5t$. We could then put the chemical potential exactly at the band touching point of the generalized Weyl cones. However, because of the large tilt of these cones, there is already a (multiband) Fermi surface for this choice of the Fermi energy, see Figure 3.4. Moreover, this Fermi surface is perfectly nested so that any instability towards fermionic superfluidity would need to compete with a charge density wave instability. This is a complicated problem which we would not like to pursue here.

Instead, we will start with a model that has generalized Weyl cones within the 1BZ, but with a point-like Fermi surface at the band touching point. To accomplish this, we add fluxes to our unit cell in a pattern that is similar to the circulating current states as was proposed by Varma for the high-T_c superconductors [12]. The difference is that we assume the fluxes to be given, meaning that they are not spontaneously formed from the interactions. This can for example be realized in optical lattices. The question is then how the emergent Bloch waves can be used for pairing in a BCS-type manner. Finally, we will also investigate the possibility of pairing when the chemical potential is put at a quadratic band touching point (QBTP). The particle-hole instabilities for such a band structure were already investigated for the Lieb lattice by Tsai *et al.* [86]. Here, we will however focus on the particle-particle channel.

4.1   Mimicking the Varma phase

In this section, we will mimic some of the Varma phases in the hope that they will give interesting band structures that can serve as a starting point for pairing instabilities. For simplicity, we will only consider Varma phase patterns that do not enlarge the unit cell, to make sure that the number of bands is minimal. In particular, we considered the circulating current phases shown in Figure 4.1. Each of these states have a flux of ϕ in a suitable plaquette within the unit cell. For example, the one shown in

Figure 4.1: Varma circulating current phases that do not enlarge the unit cell. Regarding the sublattice indices mentioned in the text, we use the same conventions as in Chapter 3.

(a) has a flux of ϕ in a $B - A - C - B$ plaquette, where we can transverse this plaquette in both clock senses. The example in (b) has a flux ϕ in a $B - C - B - C - B$ plaquette, but only when followed counterclockwise. These fluxes are realized in a tight binding model under the condition that every hopping process in the direction of an arrow is accompanied by a suitable phase factor. However, for our purposes it turns out that only (c) will be of relevance. Namely, the pattern in (a) leads to a renormalization of t' according to $t' \rightarrow t' \cos(\phi)$. The physics of such a model is already described in the previous chapter, since there we have already looked at all the possible values of t'. Pattern (b) is not interesting for fermionic superfluidity, because the effect of the flux ϕ is to create two full gaps between the three bands for $t' \neq 0$, in a similar fashion as how an intrinsic SOC acts. These gaps then host a QAHE, and topological phase transitions driven by t' can be realized here, and this was again discussed in the previous chapter. Therefore, we will only consider pattern (c). We will see that this gives us a point-like Fermi surface, which will be an interesting starting point for adding interactions.

For this pattern, the Hamiltonian can be written as

$$\hat{H}_t = -t \sum_{\langle i,j \rangle;\sigma} e^{i\theta_{i,j}} \hat{s}_{i\sigma}^\dagger \hat{s}_{j,\sigma} - t' \sum_{\langle\langle i,j \rangle\rangle;\sigma} e^{i\theta_{i,j}} \hat{s}_{i,\sigma}^\dagger \hat{s}_{j,\sigma}. \tag{4.1}$$

Here the angle $\theta_{i,j}$ has a value that depends on the particular bond that connects the sites i and j. These values are chosen such that a flux of $\pm\phi$ transverses a B-A-C-B plaquette, where the plus (minus) sign is taken if such a plaquette is transversed (counter)clockwise. Here, only NN or NNN links are considered. Moreover, we demand that the flux in an A-B-C-A-B-C-A plaquette is zero. This means that $\theta_{i,j}$ can take the values 0 or $\pm\phi/3$.

In the momentum space, we can write the Hamiltonian as $\hat{H} = \sum_{\mathbf{k},\sigma} \hat{\Psi}_{\mathbf{k},\sigma}^\dagger \mathcal{H}_{\mathbf{k}}^V \hat{\Psi}_{\mathbf{k},\sigma}$ in the basis $\hat{\Psi}_{\mathbf{k},\sigma} = (\hat{s}_{A,\mathbf{k},\sigma}, \hat{s}_{B,\mathbf{k},\sigma}, \hat{s}_{C,\mathbf{k},\sigma})$. The Hamiltonian matrix $\mathcal{H}_{\mathbf{k}}^V$ then reads

$$\mathcal{H}_{\mathbf{k}}^V = \begin{pmatrix} 0 & -2t\cos(k_x a/2 + \phi/3) & -2t\cos(k_y a/2 + \phi/3) \\ * & 0 & -4t'\cos(k_x a/2 - \phi/6)\cos(k_y a/2 - \phi/6) \\ * & * & 0 \end{pmatrix}, \tag{4.2}$$

where the asterisks '∗' need to be filled in such that the matrix is Hermitian. The factor $\phi/6$ for the term that describes hopping between the B and C sublattice is maybe not easy to understand, so let us first elaborate on this contribution. This term comes from adding the relevant phase factors, $\sum_j e^{i(\mathbf{k}\cdot\boldsymbol{\delta}_j + \theta_j)}$, where the $\boldsymbol{\delta}_j$'s are bond vectors that connect the B sites with its four NNN C sites. These vectors are given by $\boldsymbol{\delta}_1 := (\mathbf{e}_x + \mathbf{e}_y)a/2$, $\boldsymbol{\delta}_2 := -(\mathbf{e}_x + \mathbf{e}_y)a/2$, $\boldsymbol{\delta}_3 := (\mathbf{e}_x - \mathbf{e}_y)a/2$, and $\boldsymbol{\delta}_4 := -(\mathbf{e}_x - \mathbf{e}_y)a/2$. The phase θ_j is equal to $-\phi/3$ for $j = 1$, it equals $\phi/3$ for $j = 2$ and it is zero otherwise. Then we find that

$$-t' \sum_j e^{i(\mathbf{k}\cdot\boldsymbol{\delta}_j + \theta_j)} = -2t'\{\cos[(k_x + k_y)a/2 - \phi/3] + \cos[(k_x - k_y)a/2 - \phi/3]\}$$

$$= -2t'\{\cos[(k_x a/2 - \phi/6) + (k_y a/2 - \phi/6)]$$
$$+ \cos[(k_x a - \phi/6) - (k_y a/2 - \phi/6)]\}.$$

Then apply $\cos(\alpha + \beta) + \cos(\alpha - \beta) = 2\cos\alpha\cos\beta$ and the result follows.

Let us now consider some properties of the matrix in Eq.(4.2). First, we observe that this matrix reduces to $\mathcal{H}_\mathbf{k}^0$ (see previous chapter) for $\phi = 0$, as it should be. Moreover, it looks like that the Hamiltonian is 6π periodic in ϕ. However, as we shall see below, many of the band structures are equivalent up to a shift in momentum. To understand this notion, we first consider $t' = 0$. In this case, the effect of the flux is merely to displace the band structure by a vector $-(2\phi/3, 2\phi/3)$. For example, there is still a Dirac cone like structure that touches a flat middle band, but now instead of appearing at the M-point, it occurs at $(\pi - 2\phi/3, \pi - 2\phi/3)$[1]. This motivates us to define a phase dependent momentum as $q_i := k_i + 2\phi/3a$ for $i = x, y$. This definition will only be used to map out equivalent band structures onto each other. When we consider pairing later, we have to work with the original momentum $\mathbf{k}$. The Hamiltonian matrix in terms of $\mathbf{q}$ then simplifies to

$$\mathcal{H}_\mathbf{q}^V = \begin{pmatrix} 0 & -2t\cos(q_x a/2) & -2t\cos(q_y a/2) \\ * & 0 & -4t'\cos[(q_x a - \phi)/2]\cos[(q_y a - \phi)/2] \\ * & * & 0 \end{pmatrix}. \qquad (4.3)$$

From this we see that there is in fact only a 2π periodicity in ϕ, where we think of two band structures being equivalent if they can be mapped onto each other by a shift in momentum. Under this condition, the case $\phi = 0$ is equivalent to $\phi = 2\pi$. Moreover, the spectra for ϕ and $\phi + \pi$ can be mapped onto each other by a C_2 rotation. This means that we can now naturally restrict our attention to $0 \leq \phi \leq \pi$.

We observe that only for $\phi = 0$ and $\phi = \pi$ the dispersions satisfy $\epsilon(\mathbf{q}) = \epsilon(-\mathbf{q})$, because in these cases, we have that $\mathcal{H}_\mathbf{q}^V = \mathcal{H}_{-\mathbf{q}}^V$. This condition is not satisfied for other values of the flux ϕ. Despite the lack of such a symmetry, we still have that all the band touching points occur along the diagonals $q_y = \pm q_x$. The spectra along these diagonal are shown in Figure 4.2.

The dispersions still have a symmetry along the negative diagonal $q_y = -q_x$. In this case we have that $\epsilon(q_x, -q_x) = \epsilon(-q_x, q_x)$. We find band touchings between the middle and the lower bands at

---

[1]Whenever this point occurs outside the 1BZ, we have to use a reciprocal lattice vector to identify it with a point in the 1BZ.

$\pm(q_0, -q_0)$ (Figure 4.2(c)-(d)), where q_0 is given by

$$\cos(q_0) = \frac{t^2}{4t'^2} \left[1 - \frac{4t'^2}{t^2} \cos\phi - \sqrt{1 + \frac{16t'^2}{t^2} \sin^2\left(\frac{\phi}{2}\right)} \right]. \tag{4.4}$$

This solution also describes the band touching points along the positive diagonal, which occur at the points $\pm(q_0, q_0)$, see Figure 4.2(a). However, this expression is then only true for $\phi = \pi$. For all other values of the flux, there are still two Weyl cones, but not at the same energy, see Figure 4.2(b).
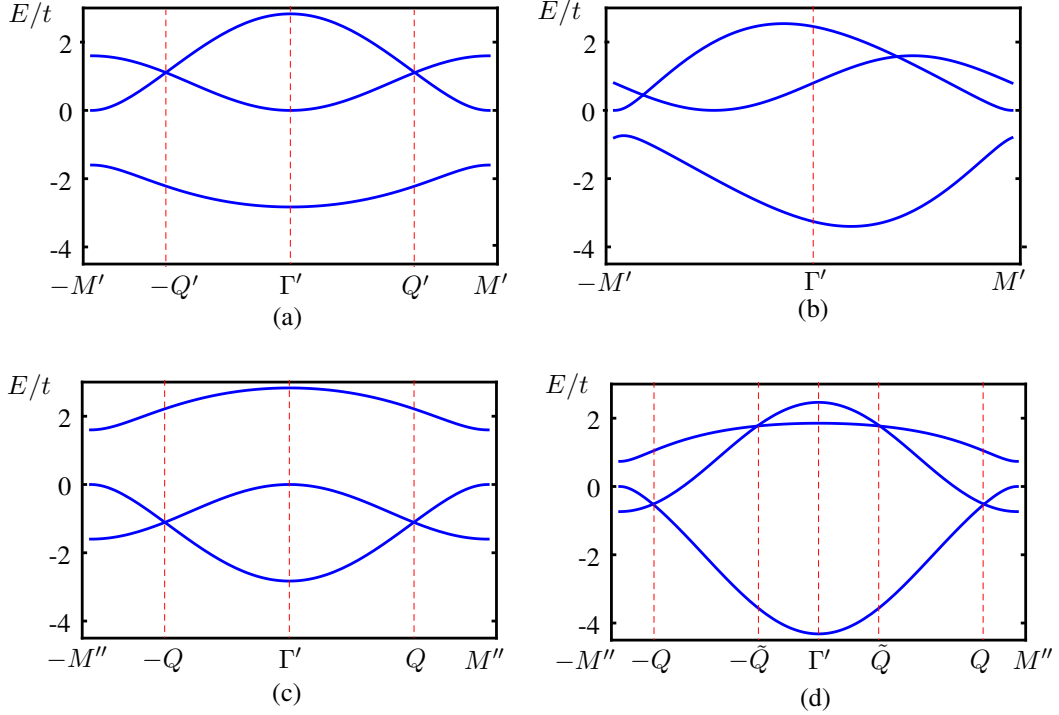
Figure 4.2: Typical band structures for Eq. (4.3) as a function of the phase dependent momentum **q**. We have defined the special points $M' = (\pi, \pi)$, $Q = (q_0, -q_0)$, $Q' = (q_0, q_0)$, $\tilde{Q} = (\tilde{q}_0, -\tilde{q}_0)$ and $\Gamma' = (0, 0)$. The upper row depicts the spectra along the positive diagonal, which show possible band touchings between the upper and the middle band, whereas the lower row depicts spectra along the negative diagonal. (a) For $\phi = \pi$, there are two Weyl points symmetrically around the zero of momentum in the shifted BZ. (b) For ϕ not an integer multiple of π, the Weyl points are not symmetrically displaced. (c) For all values of $\phi \neq 2\pi n$ (n integer), there are tunable Weyl points between the lower and the middle bands that satisfy the maximum tilt condition for all values of t'. (d) For a suitable choice of parameters, there are also Weyl touchings between the upper and the middle bands that however do not satisfy the tilt condition. The particular example shown here is for $\phi = \pi/2$ and $t' = 0.8t$.

There is also a possibility to have a band touching point between the middle band and upper band at $\pm(\tilde{q}_0, -\tilde{q}_0)$, given by the condition

$$\cos(\tilde{q}_0) = \frac{t^2}{4t'^2} \left[1 - \frac{4t'^2}{t^2} \cos\phi + \sqrt{1 + \frac{16t'^2}{t^2} \sin^2\left(\frac{\phi}{2}\right)} \right]. \tag{4.5}$$

Notice that such a band touching point does not always occur. For this to happen, it is required that the modulus of the right hand side is smaller than or equal to unity, see Figure 4.2(d).

In the following, we will always focus on the lower two band touching points. We define a vector $\mathbf{Q} := (q_0, -q_0)$, so that the two generalized Weyl cones are separated by an incommensurate vector $2\mathbf{Q}$. We are interested in putting the chemical potential at these Weyl points. In this case, the chemical potential can be found by filling in $\mathbf{Q}$ in the Hamiltonian and solve for the eigenvalues. We find that

$$\mu = \frac{t^2}{2t'} \left[-1 + \sqrt{1 + \frac{16t'^2}{t^2} \sin^2\left(\frac{\phi}{2}\right)} \right]. \tag{4.6}$$

4.2 Pairing for a circulating current pattern

We will now look at interactions and treat them in the particle-particle channel at the mean-field level. There are two types of interactions that we will consider, namely attractive on-site and NN density-density type interactions. These type of interactions can be realized with cold atoms. Although in most optical lattice experiments only on-site Hubbard interactions are realized, NN interactions are possible if one considers dipolar atoms [87], or a mixture of fermions and bosons. In the latter case, the bosons condense and the phonons of the condensate mediate a longer-range effective interaction between the fermions [88]. Before we proceed, let us look at how a MF decoupling in the particle-particle channel works.

Two-body density-density interactions are generally of the form $\hat{s}_{i,\sigma}^\dagger \hat{s}_{j,\sigma'}^\dagger \hat{s}_{j,\sigma'} \hat{s}_{i,\sigma}$. In the particle-particle channel, we expand the operators as $\hat{s}_{i,\sigma} \hat{s}_{j,\sigma'} = \langle \hat{s}_{i,\sigma} \hat{s}_{j,\sigma'} \rangle + \delta(\hat{s}_{i,\sigma} \hat{s}_{j,\sigma'})$. Here $\langle ... \rangle$ is an average taken in the grand canonical ensemble and the equality sign defines the fluctuations around this average value. Inserting this expansion in the interaction term, we find that

$$\begin{aligned} \hat{s}_{i,\sigma}^\dagger \hat{s}_{j,\sigma'}^\dagger \hat{s}_{j,\sigma'} \hat{s}_{i,\sigma} &= \left(\langle \hat{s}_{i,\sigma'}^\dagger \hat{s}_{j,\sigma'}^\dagger \rangle + \delta(\hat{s}_{i,\sigma}^\dagger \hat{s}_{j,\sigma'}^\dagger) \right) \left(\langle \hat{s}_{j,\sigma'} \hat{s}_{i,\sigma} \rangle + \delta(\hat{s}_{j,\sigma'} \hat{s}_{i,\sigma}) \right) \\ &\approx \langle \hat{s}_{i,\sigma'}^\dagger \hat{s}_{j,\sigma'}^\dagger \rangle \hat{s}_{j,\sigma'} \hat{s}_{i,\sigma} + \hat{s}_{i,\sigma'}^\dagger \hat{s}_{j,\sigma'}^\dagger \langle \hat{s}_{j,\sigma'} \hat{s}_{i,\sigma} \rangle - \langle \hat{s}_{i,\sigma'}^\dagger \hat{s}_{j,\sigma'}^\dagger \rangle \langle \hat{s}_{j,\sigma'} \hat{s}_{i,\sigma} \rangle. \end{aligned} \tag{4.7}$$

We shall now apply this to specific cases.

4.2.1 On-site interactions

Let us consider first the simple case of an attractive on-site interaction of the form

$$\hat{H}_{\text{int}} = -U \sum_i \hat{s}_{i,\uparrow}^\dagger \hat{s}_{i,\downarrow}^\dagger \hat{s}_{i,\downarrow} \hat{s}_{i,\uparrow}, \tag{4.8}$$

with $U > 0$. After the mean-field decoupling, we find

$$\hat{H}_{\text{int}}^{\text{MF}} = \frac{3N|\Delta|^2}{U} - \sum_i \left(\hat{s}_{i,\uparrow}^\dagger \hat{s}_{i,\downarrow}^\dagger \Delta + \text{h.c.} \right), \tag{4.9}$$

with respect to the order parameter $\Delta = U\langle \hat{s}_{i,\downarrow} \hat{s}_{i,\uparrow} \rangle$ and where N is the number of unit cells. The factor three arises because there are three sublattices in each unit cell. Moreover, notice that for simplicity we assume our order parameter to be site independent and we absorb U in its definition to make sure that it has the dimension of energy. It is now straightforward to write (4.9) in momentum space. We then arrive at the mean-field (MF) Hamiltonian $\hat{H}_{\text{MF}} := \hat{H}_t + \hat{H}_{\text{int}}^{\text{MF}}$, which in the grand canonical ensemble can be written in the form

$$\hat{H}_{\text{MF}} - \mu \hat{N} = \sum_{\mathbf{k}} (\hat{\Psi}_{\mathbf{k},\uparrow}^\dagger, \hat{\Psi}_{-\mathbf{k},\downarrow}) \mathcal{H}_{\mathbf{k}}^{\text{BdG}} \begin{pmatrix} \hat{\Psi}_{\mathbf{k},\uparrow} \\ \hat{\Psi}_{-\mathbf{k},\downarrow}^\dagger \end{pmatrix} - \sum_{\mathbf{k}} 3\mu + \frac{3N|\Delta|^2}{U}, \tag{4.10}$$

with the 6×6 Bogoliubov-de Gennes (BdG) Hamiltonian matrix given by

$$\mathcal{H}_{\mathbf{k}}^{\text{BdG}} = \begin{pmatrix} \mathcal{H}_{\mathbf{k}}^V - \mu \mathbb{1}_{3\times3} & -\Delta \mathbb{1}_{3\times3} \\ -\Delta^* \mathbb{1}_{3\times3} & -\mathcal{H}_{-\mathbf{k}}^V + \mu \mathbb{1}_{3\times3} \end{pmatrix}. \tag{4.11}$$

Notice that this matrix is by construction particle-hole symmetric. Before we start diagonalizing $\mathcal{H}_{\mathbf{k}}^{\text{BdG}}$, let us comment on the other contributions in (4.11). We see that there is a term proportional to μ that does not depend on the order parameters. Such a term arises because we used the anti-commutation relations to write $\hat{s}_{X,-\mathbf{k},\downarrow}^\dagger \hat{s}_{X,-\mathbf{k},\downarrow} = 1 - \hat{s}_{X,-\mathbf{k},\downarrow} \hat{s}_{X,-\mathbf{k},\downarrow}^\dagger$. Moreover, the sum over wavenumbers is convergent because of the ultraviolet cut-off imposed by the lattice constant. This term can in principle be neglected because it does not depend on the order parameters, in contrast to the last term.

We will now proceed to diagonalize $\mathcal{H}_{\mathbf{k}}^{\text{BdG}}$. However, it is difficult to find the eigenvalues explicitly. First of all, the characteristic polynomial is of degree six and it is involved to find the roots since $\mathcal{H}_{\mathbf{k}}^V \neq \mathcal{H}_{-\mathbf{k}}^V$. If this would not be the case, then $\left(\mathcal{H}_{\mathbf{k}}^{\text{BdG}} \right)^2$ would be block diagonal and it would be easy to find the eigenvalues using Cardano's method, because the sextic characteristic polynomial would then factorize into two cubics. Unfortunately this is not true, so the eigenvalues have to be found numerically.

However, the above fact has a non-trivial consequence. To see this, let us consider the unitary transformation such that the non-interacting Hamiltonian is diagonal, i.e., we transform the operators to the band representation. This unitary transformation can be written as $\Lambda_{\mathbf{k}} = Q_{\mathbf{k}} \mathcal{H}_{\mathbf{k}}^V Q_{\mathbf{k}}^\dagger$, where $\Lambda_{\mathbf{k}}$ is a diagonal matrix that consists of the eigenvalues of $\mathcal{H}_{\mathbf{k}}^V$. It is interesting to apply such a transformation to the BdG Hamiltonian matrix. This is done by $W_{\mathbf{k}} = \text{diag}(Q_{\mathbf{k}}, Q_{-\mathbf{k}})$ according to $\mathcal{H}_{\mathbf{k}}^{\text{BdG}} \rightarrow W_{\mathbf{k}} \mathcal{H}_{\mathbf{k}}^{\text{BdG}} W_{\mathbf{k}}^\dagger$. We find

$$W_{\mathbf{k}} \mathcal{H}_{\mathbf{k}}^{\text{BdG}} W_{\mathbf{k}}^\dagger = \begin{pmatrix} Q_{\mathbf{k}} \mathcal{H}_{\mathbf{k}}^V Q_{\mathbf{k}}^\dagger - \mu \mathbb{1}_{3\times3} & -\Delta Q_{\mathbf{k}} Q_{-\mathbf{k}}^\dagger \\ -\Delta^* Q_{-\mathbf{k}} Q_{\mathbf{k}}^\dagger & -Q_{-\mathbf{k}} \mathcal{H}_{-\mathbf{k}}^V Q_{-\mathbf{k}}^\dagger + \mu \mathbb{1}_{3\times3} \end{pmatrix} \tag{4.12}$$

$$= \begin{pmatrix} \Lambda_{\mathbf{k}} - \mu \mathbb{1}_{3\times3} & -\Delta Q_{\mathbf{k}} Q_{-\mathbf{k}}^\dagger \\ -\Delta^* Q_{-\mathbf{k}} Q_{\mathbf{k}}^\dagger & -\Lambda_{-\mathbf{k}} + \mu \mathbb{1}_{3\times3} \end{pmatrix}. \tag{4.13}$$

Notice that the condition $\mathcal{H}_{\mathbf{k}}^V \neq \mathcal{H}_{-\mathbf{k}}^V$ implies that we have that $Q_{\mathbf{k}}Q_{-\mathbf{k}}^\dagger \neq \mathbb{1}_{3\times 3}$. This mean that the on-site pairing naturally leads to intra-band and inter-band pairing, in sharp contrast to the case if the Hamiltonian is symmetric under $\mathbf{k} \to -\mathbf{k}$. In such a case, we would only have intraband pairing.

Now, suppose we know the eigenvalues. Then, we can write the Hamiltonian in the basis in which it is diagonal. This is accompanied by a unitary transformation $U_{\mathbf{k}}$, in which the Nambu spinor is transformed to the quasi-particle basis

$$\begin{pmatrix} \hat{\Upsilon}_{\mathbf{k},\uparrow} \\ \hat{\Upsilon}_{-\mathbf{k},\downarrow}^\dagger \end{pmatrix} = U_{\mathbf{k}} \begin{pmatrix} \hat{\Psi}_{\mathbf{k},\uparrow} \\ \hat{\Psi}_{-\mathbf{k},\downarrow}^\dagger \end{pmatrix}, \tag{4.14}$$

with the three-component quasi-particle spinor given by $\hat{\Upsilon}_{\mathbf{k},\sigma} := (\hat{\varsigma}_{1,\mathbf{k},\sigma}, \hat{\varsigma}_{2,\mathbf{k},\sigma}, \hat{\varsigma}_{3,\mathbf{k},\sigma})$. Then, we can write $U_{\mathbf{k}}\mathcal{H}_{\mathbf{k}}^{\mathrm{BdG}}U_{\mathbf{k}}^\dagger = \mathrm{diag}(E_{1,\mathbf{k}}, E_{2,\mathbf{k}}, E_{3,\mathbf{k}}, -E_{1,-\mathbf{k}}, -E_{2,-\mathbf{k}}, -E_{3,-\mathbf{k}})$, where we used the particle-hole symmetry. In terms of the quasi-particle creation and annihilation operators, the MF Hamiltonian becomes

$$\hat{H}_{\mathrm{MF}} - \mu\hat{N} = \sum_{\mathbf{k},\sigma}\sum_{i=1}^3 E_{i,\mathbf{k}}\hat{\varsigma}_{i,\mathbf{k},\sigma}^\dagger\hat{\varsigma}_{i,\mathbf{k},\sigma} - \sum_{\mathbf{k}}\left(3\mu + \sum_{i=1}^3 E_{i,\mathbf{k}}\right) + \frac{3N|\Delta|^2}{U}. \tag{4.15}$$

The terms in the above equation have the same interpretation as in the conventional BCS theory. The first term takes into account quasi-particle excitations, while the other terms denote the energy of the vacuum for the quasi-particles. The theory is now free, so it is straightforward to calculate the partition function

$$Z_{\mathrm{MF}} = \mathrm{Tr}\left[e^{-\beta(\hat{H}-\mu\hat{N})}\right] = e^{-3\beta N|\Delta|^2/U}\prod_{\mathbf{k},\sigma} e^{\beta(3\mu+\sum_i E_{i,\mathbf{k}})/2}\left(1 + e^{-\beta\sum_i E_{i,\mathbf{k}}}\right). \tag{4.16}$$

The factor $1/2$ in the exponent arises because we included this term inside the product over σ, which takes two values. From this, we can calculate the grand potential

$$\Omega_{\mathrm{MF}} = -\beta^{-1}\log Z_{\mathrm{MF}} = \frac{3N|\Delta|^2}{U} - \sum_{\mathbf{k},\sigma}\left[(3\mu + \sum_i E_{i,\mathbf{k}})/2 + \beta^{-1}\log\left(1 + e^{-\beta\sum_i E_{i,\mathbf{k}}}\right)\right]. \tag{4.17}$$

Let us assume that $E_{i,\mathbf{k}} \geq 0$. We are interested in the case $T \to 0$ (or equivalently $\beta \to \infty$), in the thermodynamic limit. If we neglect all terms independent of Δ, then the grand potential per unit cell reads

$$\omega := \frac{\Omega_{\mathrm{MF}}}{N} = \frac{3|\Delta|^2}{U} - \int_{\mathrm{1BZ}}\frac{d^2\mathbf{k}}{(2\pi)^2}\sum_i E_i(\mathbf{k}). \tag{4.18}$$

In finding this expression, we used that the total system surface is N, in units where $a = 1$. Normally, we can find the gap equations by setting the derivative of this quantity with respect to Δ equal to zero. This is equivalent to evaluate the self-consistency condition $\Delta = U\langle\hat{s}_{i,\downarrow}\hat{s}_{i,\uparrow}\rangle$. However, because we do not have analytical expressions for the quasi-particle dispersions, it is more feasible to minimize ω numerically.

We have performed such minimization for, e.g., $\phi = \pi$ and $t' = 0.4t$, where we assumed Δ to be real. What we observe is that there is a second-order phase transition to a superfluid phase at a critical coupling of $U_c \approx 5t$. The fact that a critical coupling is needed for a phase transition to occur
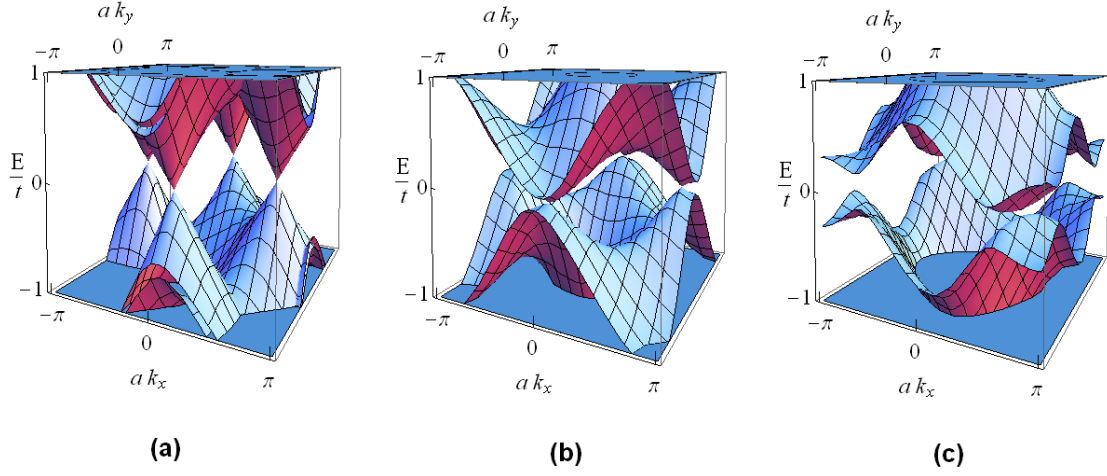
Figure 4.3: Quasiparticle spectra when on-site pairing Δ is included. Only the spectra near $E = 0$ are shown. In these examples, we have taken $\phi = \pi$ and $t' = 0.4t$. (a) For $\Delta = 0$ the spectra are gapless in the 1BZ. (b) For $\Delta = t$ the spectra are still gapless, but now at different points in the 1BZ. (c) A full superfluid gap is formed when Δ is sufficiently large. In this example, we have put $\Delta = 2t$.

at $T = 0$ does not come as a surprise. Indeed, this is because of a vanishing density of states (DOS) at the Weyl points. Such a behaviour was already observed earlier for proposals of superconductivity in graphene [89] and on a square lattice with a staggered flux [88], when the chemical potential is at the Dirac point. Finally, we checked how the critical value of the coupling depends on the separation of the Weyl points, which can be tuned by t' and ϕ. We found that this has minimal influence, so that U_c is almost a constant as function of t' and ϕ.

Because the phase transition is second-order, this means that in principle we have access to various values of the order parameter Δ. For sufficiently strong interaction, the weak coupling calculation that we have performed here would not hold. Still, let us consider the various quasiparticle excitation spectra that can occur as a function of Δ. Then, we find something remarkable: for a non-zero value of Δ, the quasiparticle spectrum is not necessarily gapped in the full 1BZ, see Figure 4.3(b). Only if Δ is sufficiently large, a superfluid gap can occur, see Figure 4.3(c). This is rather strange, because normally on-site pairing immediately opens a gap in the spectrum. We do not quite understand this observation, but it may be due to the interband components in the on-site pairing. Arguably, this makes it harder to gap out the quasiparticle branches. Moreover, we see that tuning Δ can move around the points for which the spectrum is gapless, before a superfluid gap opens.

4.2.2 Nearest-neighbour interactions

We now add a nearest neighbour attraction term of the form

$$\hat{H}_{\text{int}} = -\frac{V}{2} \sum_{\langle i,j \rangle} \sum_{\sigma,\sigma'} \hat{s}_{i,\sigma}^\dagger \hat{s}_{j,\sigma'}^\dagger \hat{s}_{j,\sigma'} \hat{s}_{i,\sigma}, \tag{4.19}$$

where $V > 0$. The factor $1/2$ is to avoid double counting. However, we could also have chosen to restrict the sum over the sites in the A sublattice and then sum over the four possible NN of such a site. We checked that this would give us the same result. Next, we decouple this interaction term in the particle-particle channel to find the mean field correction to the Hamiltonian

$$\hat{H}_{\text{int}} \approx E_0 - \sum_{\langle i,j \rangle} \sum_{\sigma,\sigma'} \left(\hat{s}^{\dagger}_{i,\sigma} \hat{s}^{\dagger}_{j,\sigma'} \Delta_{j,i;\sigma',\sigma} + \text{h.c.} \right), \tag{4.20}$$

with $E_0 := \sum_{\langle i,j \rangle} \sum_{\sigma,\sigma'} |\Delta_{i,j;\sigma,\sigma'}|^2/V$. The question is now how we should define our order parameters. There are various possibilities to do this. First, notice that the $\Delta_{i,j;\sigma,\sigma'} = V \langle \hat{s}_{i,\sigma} \hat{s}_{j,\sigma'} \rangle$ denote particle-particle correlations across a bond in the lattice connecting two nearest-neighbour sites. One way is then to define a spin-singlet order parameter, for which we allow the value to depend on the particle bond. Such an approach was already discussed for graphene [90] and for the square lattice under a staggered flux [88]. This type of order parameters has a RVB-like character, that may lead to unconventional order parameters that are worthwhile to consider. Here, we will however adopt a different approach, as proposed by Roy and Herbut [91].

For simplicity, let us first assume that the values of the bond order parameters are equal for the four bonds around an A site. Moreover, if the chemical potential is chosen such that there is a point-like Fermi surface, it leads to a phenomenon that is called hidden order. This was proposed for graphene [89], where tuning the NN gap parameters does not open a gap at the Dirac point. Instead, one renormalizes the Fermi velocity. Roy and Herbut elaborated on this fact by choosing a particular ansatz appropriate to the honeycomb lattice for the NN pairing parameters [91]. By connecting the two Dirac cones in the 1BZ by a commensurate separation vector $\mathbf{K}$, they proposed an FFLO state for the spin triplet part of the decoupling: a superconducting state that is spatially inhomogeneous, but periodic with $2\mathbf{K}$. Such states were first proposed by Fulde, Ferrell, Larkin and Ovchinnikov [92, 93] and they describe pairing at a finite momentum. Namely, in standard BCS theory, the state $(\mathbf{k}, \uparrow)$ is paired with $(-\mathbf{k}, \downarrow)$, while in the FFLO state we have pairing between $(\mathbf{k} + \mathbf{K}, \uparrow)$ and $(-\mathbf{k} + \mathbf{K}, \downarrow)$, so that the Cooper pair has total momentum $2\mathbf{K}$.

In the case of the honeycomb lattice, such a pairing ansatz leads to a so-called Kekule pattern. In a suitable parameter regime this pattern is more favourable than the hidden order that would result from the spin singlet part of the decoupling. In principle, we are interested in employing such a 'Kekule' ansatz here, which means that we connect the two Weyl points with the vector $2\mathbf{Q}$. However, we will not solve this problem for the Lieb lattice in this thesis, but we will comment on the differences at the end of this section. For now, let us just consider their ansatz and look at what kind of contributions we can expect. We define the order parameters as

$$\Delta_{i,j;\sigma,\sigma} = \Delta_{\sigma} \cos[\mathbf{Q} \cdot (\mathbf{x}_i + \mathbf{x}_j) + \alpha],$$

$$\frac{1}{2}(\Delta_{i,j;\downarrow\uparrow} + \Delta_{i,j;\uparrow\downarrow}) = \tilde{\Delta} \cos[\mathbf{Q} \cdot (\mathbf{x}_i + \mathbf{x}_j) + \alpha],$$

$$\frac{1}{2}(\Delta_{i,j;\downarrow\uparrow} - \Delta_{i,j;\uparrow\downarrow}) = \Delta'.$$

Here, α parametrizes various possible inhomogeneous superfluid states for the components of the

triplet. Using this ansatz, we find that

$$\sum_{\sigma,\sigma'} \hat{s}_{i,\sigma}^\dagger \hat{s}_{j,\sigma'}^\dagger \Delta_{j,i;\sigma',\sigma} = \sum_\sigma \Delta_\sigma \cos[\mathbf{Q} \cdot (\mathbf{x}_i + \mathbf{x}_j) + \alpha] \hat{s}_{i,\sigma}^\dagger \hat{s}_{j,\sigma}^\dagger$$
$$+ \tilde{\Delta} \cos[\mathbf{Q} \cdot (\mathbf{x}_i + \mathbf{x}_j) + \alpha](\hat{s}_{i,\uparrow}^\dagger \hat{s}_{j,\downarrow}^\dagger + \hat{s}_{i,\downarrow}^\dagger \hat{s}_{j,\uparrow}^\dagger) + \Delta'(\hat{s}_{i,\uparrow}^\dagger \hat{s}_{j,\downarrow}^\dagger - \hat{s}_{i,\downarrow}^\dagger \hat{s}_{j,\uparrow}^\dagger) \tag{4.21}$$

We are now interested in how these terms look like in the momentum space. For example, suppressing the spin indices, we find

$$\sum_{\langle i,j \rangle} \cos[\mathbf{Q} \cdot (\mathbf{x}_i + \mathbf{x}_j) + \alpha] \hat{s}_i^\dagger \hat{s}_j^\dagger = \sum_{\mathbf{k}} \{ \hat{s}_{A,\mathbf{k}-\mathbf{Q}}^\dagger \hat{s}_{B,-\mathbf{k}-\mathbf{Q}}^\dagger \cos[(k_x + Q_x)/2] e^{i\alpha}$$
$$+ \hat{s}_{A,\mathbf{k}+\mathbf{Q}}^\dagger \hat{s}_{B,-\mathbf{k}+\mathbf{Q}}^\dagger \cos[(k_x - Q_x)/2] e^{-i\alpha} \} + (B \to C, x \to y),$$

where we have performed a shift in the first term $\mathbf{k} \to \mathbf{k} - \mathbf{Q}$ and in the second term $\mathbf{k} \to \mathbf{k} + \mathbf{Q}$. Finally, we rewrite E_0 using this ansatz,

$$E_0 = \frac{N}{V}(4|\Delta'|^2 + 2|\tilde{\Delta}|^2 + |\Delta_\uparrow|^2 + |\Delta_\downarrow|^2), \tag{4.22}$$

where for the last three terms we have used that $\mathbf{Q}$ is not a reciprocal lattice vector.

4.2.3 Hidden order

With the calculations performed in the previous subsection, it is now possible to write down the BdG Hamiltonian. Let us do this for a simple case, where we assume $\tilde{\Delta} = \Delta_\uparrow = \Delta_\downarrow = 0$. It is then straightforward to write down the Hamiltonian

$$\hat{H}_{\text{MF}} - \mu \hat{N} = \sum_{\mathbf{k}} (\hat{\Psi}_{\mathbf{k},\uparrow}^\dagger, \hat{\Psi}_{-\mathbf{k},\downarrow}) \mathcal{H}_{\mathbf{k}}^{\text{BdG}} \begin{pmatrix} \hat{\Psi}_{\mathbf{k},\uparrow} \\ \hat{\Psi}_{-\mathbf{k},\downarrow}^\dagger \end{pmatrix} - \sum_{\mathbf{k}} 3\mu + E_0, \tag{4.23}$$

with the 6×6 Bogoliubov-de Gennes (BdG) Hamiltonian matrix given by

$$\mathcal{H}_{\mathbf{k}}^{\text{BdG}} = \begin{pmatrix} \mathcal{H}_{\mathbf{k}}^V - \mu \mathbb{1}_{3\times 3} & \mathcal{P}_{\mathbf{k}} \\ \mathcal{P}_{\mathbf{k}}^\dagger & -\mathcal{H}_{-\mathbf{k}}^V + \mu \mathbb{1}_{3\times 3} \end{pmatrix}. \tag{4.24}$$

Here, the pairing matrix $\mathcal{P}_{\mathbf{k}}$ is given by

$$\mathcal{P}_{\mathbf{k}} = -\Delta' \begin{pmatrix} 0 & c_x & c_y \\ c_x & 0 & 0 \\ c_y & 0 & 0 \end{pmatrix}. \tag{4.25}$$

Notice that this matrix is proportional to the non-interacting Hamiltonian for $\phi = 0$ and $t' = 0$. In some sense, this is the same as the hidden order proposed for graphene, where the pairing matrix had the same $\mathbf{k}$ dependent coefficients as the non-interacting part of the Hamiltonian. Indeed, by numerically diagonalizing $\mathcal{H}_{\mathbf{k}}^{\text{BdG}}$ we find that Δ' is not able to create a gap in the spectrum at zero energy. However, in contrast to the graphene case, it not only renormalizes the Fermi velocity, but
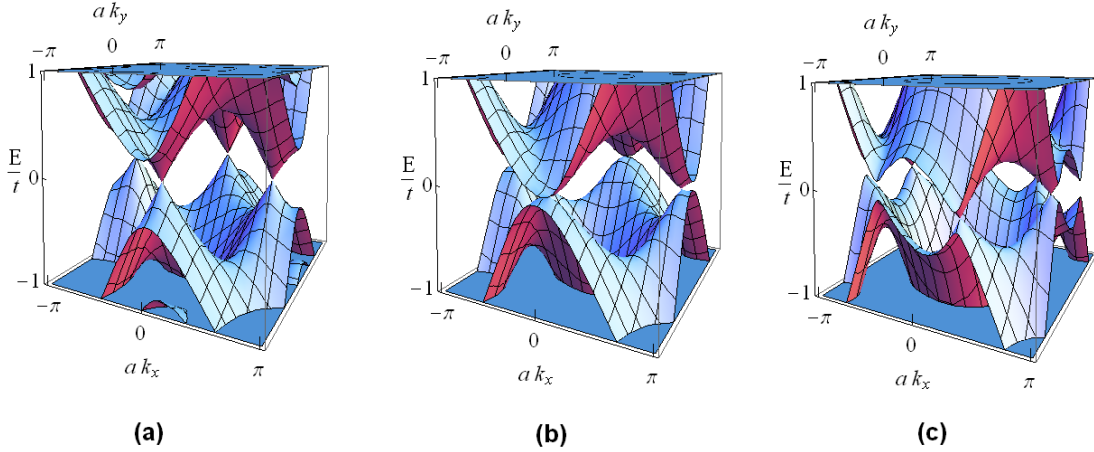
Figure 4.4: Quasiparticle spectra when NN pairing Δ' is included. Only the spectra near $E = 0$ are shown. In these examples, we have taken $\phi = \pi$ and $t' = 0.4t$. (a) For $\Delta = 0.5t$ the spectra are gapless in the 1BZ, but at different points than for $\Delta' = 0$, see Figure 4.3(a). The points for which the spectra are gapless depends on the value of Δ'. For example, in (b), we have $\Delta' = t$ and in (c) we have put $\Delta' = 2t$.

also the position of the points in the BZ for which there is no gap, see Figure 4.4. Finally, we note that by minimizing the relevant grand potential per unit cell ω, we find that a critical interaction $V_c \approx 9t$ is needed (assuming Δ' to be real), before a fermionic superfluid can form. The phase transition is then second order, and again, all of this seems to be independent of the separation of the Weyl cones.

4.2.4 FFLO state on the Lieb lattice: a small outlook

Let us now comment on how the BdG Hamiltonian matrix would look like if the FFLO state is taken into account. Then a six-component spinor will not suffice. We need to choose a 24-component Nambu spinor as follows

$$\hat{\Phi}_{\mathbf{k}} = (\hat{\Psi}_{\mathbf{k}+\mathbf{Q},\uparrow}, \hat{\Psi}_{\mathbf{k}+\mathbf{Q},\downarrow}, \hat{\Psi}_{\mathbf{k}-\mathbf{Q},\uparrow}, \hat{\Psi}_{\mathbf{k}-\mathbf{Q},\downarrow}, \hat{\Psi}^{\dagger}_{-\mathbf{k}-\mathbf{Q},\uparrow}, \hat{\Psi}^{\dagger}_{-\mathbf{k}-\mathbf{Q},\downarrow}, \hat{\Psi}^{\dagger}_{-\mathbf{k}+\mathbf{Q},\uparrow}, \hat{\Psi}^{\dagger}_{-\mathbf{k}+\mathbf{Q},\downarrow}). \tag{4.26}$$

The Hamiltonian can then be written as

$$\hat{H}_{\mathrm{MF}} - \mu \hat{N} = \sum_{\mathbf{k}} \hat{\Phi}^{\dagger}_{\mathbf{k}} \mathcal{H}^{\mathrm{BdG}}_{\mathbf{k}} \hat{\Phi}_{\mathbf{k}} - \sum_{\mathbf{k}} 3\mu + E_0, \tag{4.27}$$

where now $\mathcal{H}^{\mathrm{BdG}}_{\mathbf{k}}$ is a 24×24 matrix. We have yet to diagonalize this matrix, but we can already comment on some differences with the Kekule superconductor for graphene. First of all, the size of the matrix can be understood by counting the degrees of freedom for valley (2), spin (2), sublattice (3) and finally from the Nambu space construction (2). The amount of sublattices (three instead of two) makes this a bigger matrix than was found for graphene, where it was 16×16.

There are also other differences between the Lieb lattice and graphene. In graphene, the Dirac cones are situated at the high symmetry points. Moreover, the wavenumbers of these cones add up to

zero. This is in contrast to the Weyl cones in our case, because they are not centered symmetrically around the Γ point. Moreover, the vector that connects them is incommensurate, while for graphene the separation vector is commensurate. This means that for the Lieb lattice, no simple interpretation can be given for the superfluid phase in terms of a Kekule pattern. Finally, and most importantly, the Weyl cones are tunable. In principle, their position in the 1BZ can vary, which means that a low-energy approximation is questionable. We already saw that this could occur in the previous subsections. In the graphene case, the Dirac cones were always at the same point because they are protected. This allowed Roy and Herbut [91] to perform a low-energy approximation. By the use of symmetries, it was then straightforward to solve for the eigenvalues of their 16×16 matrix. It seems that our system has little symmetry that we can really use. This makes the FFLO state with a Varma phase pattern a highly non-trivial problem. However, we may want to pursue this problem as a future work.

4.3 Pairing for a quadratic band touching point

The absence of symmetries make the problem of the previous section very difficult. Nevertheless, it is an interesting scenario because of the presence of two Weyl cones in the 1BZ that allowed an FFLO type ansatz. We can generate more types of non-interacting band structures on the Lieb lattice with a point-like Fermi surface for a suitable choice of the Fermi level. As another example, we will consider the quadratic band touching point. It occurs if a local chemical potential ϵ_A on the A sublattice is included and if we allow for a third-nearest-neighbour hopping t'', with the restriction that such a hopping process cannot cross another lattice site, see Figure 3.1(a).

Hartree-Fock (i.e., particle-hole) like mean-field corrections from repulsive interactions were considered by Tsai and collaborators [86] . They found that the QBTP is then unstable towards various nematic, QSH and QAH phases driven by the repulsive interactions. Our approach would be different, because we will look at attractive interactions in the particle-particle channel. Moreover, we will only briefly discuss the possibilities.

4.3.1 Non-interacting case

We define the spinor $\hat{\Psi}_{\mathbf{k},\sigma} := (\hat{s}_{A,\mathbf{k},\sigma}, \hat{s}_{B,\mathbf{k},\sigma}, \hat{s}_{C,\mathbf{k},\sigma})$, to write down the non-interacting Hamiltonian as

$$\hat{H}_t = \sum_{\mathbf{k},\sigma} \hat{\Psi}^\dagger_{\mathbf{k},\sigma} \mathcal{H}^{\mathrm{QB}}_{\mathbf{k}} \hat{\Psi}_{\mathbf{k},\sigma}, \tag{4.28}$$

with

$$\mathcal{H}^{\mathrm{QB}}_{\mathbf{k}} = \begin{pmatrix} \epsilon_A & -2tc_x & -2tc_y \\ -2tc_x & -2t''c_{2y} & -4t'c_xc_y \\ -2tc_y & -4t'c_xc_y & -2t''c_{2x} \end{pmatrix}, \tag{4.29}$$

where we abbreviated $c_{\gamma i} := \cos(\gamma k_i a/2)$ for $i = x, y$ and $\gamma = 1, 2$. For $\epsilon_A < 0$ and $t'' \neq 0$ there is a QBTP at M, where both bands have opposite curvature. This is the case that we are interested in and this is shown in Figure 4.5.
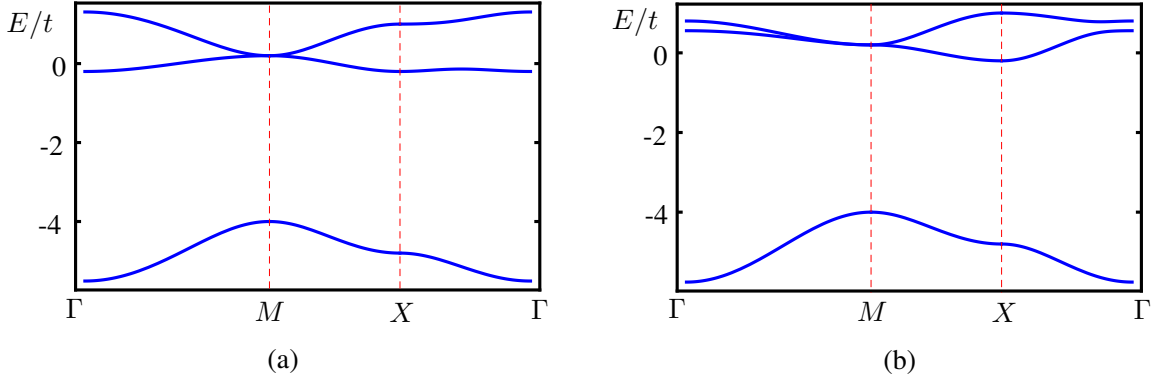
Figure 4.5: Quadratic band touching point for $\epsilon_A = -4t$ and $t'' = 0.1t$. (a) For the case $t' = 0$ and when $t' = 0.25t$. The effect of NNN hopping is thus to change the curvatures of the two bands at the M point. However for suitably large t' we end up in the same behaviour as in (a).

We will now look at the low-energy structure of this QBTP. At the M point, the eigenvalues of $\mathcal{H}_{\mathbf{k}}^{\mathrm{QB}}$ are given by ϵ_ν^0 with $\nu = 1, 2, 3$ and corresponding eigenvectors $|\psi_\nu\rangle$. Let us label the bands such that $\nu = 3$ corresponds to the band that is gapped out. We define $\mathbf{k} = \mathbf{k}_M + \mathbf{p}$ and we use this to expand the Hamiltonian matrix entrywise, $\mathcal{H}^{\mathrm{QB}} \simeq \mathcal{H}^{\mathrm{QB}}(\mathbf{k}_m) + \delta\mathcal{H}(\mathbf{p})$ to quadratic order. By using the Luttinger-Kohn representation at the point $\mathbf{k}_M$, we find the matrix elements of the effective Hamiltonian $\mathcal{H}^{\mathrm{eff}}$

$$\mathcal{H}_{\nu,\nu'}^{\mathrm{eff}} = \epsilon_\nu^0 \delta_{\nu,\nu'} + \langle\psi_\nu|\delta\mathcal{H}_{\mathbf{p}}|\psi_{\nu'}\rangle + \frac{1}{2}\langle\psi_\nu|\delta\mathcal{H}_{\mathbf{p}}|\psi_3\rangle\langle\psi_3|\delta\mathcal{H}_{\mathbf{p}}|\psi_{\nu'}\rangle\left(\frac{1}{\epsilon_\nu^0 - \epsilon_3^0} + \frac{1}{\epsilon_{\nu'}^0 - \epsilon_3^0}\right), \quad (4.30)$$

with $\nu, \nu' = 1, 2$. The result is

$$\mathcal{H}^{\mathrm{eff}}(\mathbf{p}) = \begin{pmatrix} m_0^{-1}p_x^2 - t''p_y^2 & p_xp_y(m_0^{-1} - t') \\ p_xp_y(m_0^{-1} - t') & m_0^{-1}p_y^2 - t''p_x^2 \end{pmatrix}, \quad (4.31)$$

with $m_0^{-1} := t^2/(t'' - \epsilon_A)$. Here, we put the zero of energy at the band touching point, which means that we neglected all terms that do not depend on $\mathbf{p}$. This effective Hamiltonian can then be rewritten in terms of the identity matrix $\sigma_0 := \mathbb{1}$ and the Pauli matrices $\boldsymbol{\sigma} := (\sigma_1, \sigma_2, \sigma_3)$ as $\mathcal{H}^{\mathrm{eff}}(\mathbf{p}) = \sum_{\mu=0}^3 f_\mu(\mathbf{p})\sigma_\mu$, with the coefficients given by

$$f_0(\mathbf{p}) = \frac{1}{2}(p_x^2 + p_y^2)(m_0^{-1} - t''), \quad (4.32)$$

$$f_1(\mathbf{p}) = p_xp_y(m_0^{-1} - t'), \quad (4.33)$$

$$f_2(\mathbf{p}) = 0, \quad (4.34)$$

$$f_3(\mathbf{p}) = \frac{1}{2}(p_x^2 - p_y^2)(m_0^{-1} + t''). \quad (4.35)$$

In terms of these coefficients, the dispersion around the M-point is easily found to be

$$\epsilon_\pm(\mathbf{p}) = f_0(\mathbf{p}) \pm \sqrt{f_1(\mathbf{p})^2 + f_3(\mathbf{p})^2}. \quad (4.36)$$

The fact that $f_\mu(\mathbf{p}) = f_\mu(-\mathbf{p})$ for $\mu = 0,..,4$, implies that $\epsilon_\pm(\mathbf{p}) = \epsilon_\pm(-\mathbf{p})$. Moreover, the two bands are particle-hole symmetric only for the case that $f_0(\mathbf{p}) = 0$. Finally, for a certain set of parameters, $\epsilon_\pm(\mathbf{0})$ can be either a saddle point, maximum or minimum. This is controlled by t' for the QBTP that we consider here. This is not explicitly discussed by Tsai *et al.* [86] because they have neglected the contribution of t'. However, for a suitable choice of $t' > t''$, it can be made sure that it is roughly the same band touching point as if $t' = 0$. This indeed allows us to neglect t', if we are only interested in quadratic bands that touch with opposite curvature.

4.3.2 A small note on the effect of attractive interactions

In a sense, the above non-interacting Hamiltonian is easier to handle than the Varma case because the position of the QBTP is protected and more symmetries are present. One example of such a symmetry is that $\mathcal{H}_\mathbf{k}^{QB}$ is invariant under inversion. As was discussed previously, this means that an on-site pairing with equal amplitude on the various sublattices would only induce intraband pairing. This leads to a gapped superfluid for every value of the on-site order parameter. The second difference with the Varma case is that the instability already occurs for an infinitesimal attractive interaction. The absence of a critical interaction strength at zero temperature is because the DOS does not vanish at the QBTP. Moreover, this allows us to have more control over the types of superfluid phases that may occur, because we have more control over the range in which the weak coupling approach is valid.

A pairing instability that would result from an on-site interaction is not particularly interesting in this case. Instead, we will consider NN and NNN interactions, where we parametrize the latter with a constant $W > 0$. Just like in the Varma case, we need to think about the definition of the order parameters. Here the FFLO ansatz is not possible because there is only one QBTP in the 1BZ. However, we can still consider an RVB-type order parameter, for which we allow the values of the various bond order parameters to vary. In such a case, the BdG Hamiltonian matrix takes the form

$$\mathcal{H}_\mathbf{k}^{BdG} = \begin{pmatrix} \mathcal{H}_\mathbf{k}^{QB} - \mu \mathbb{1}_{3\times 3} & \mathcal{P}_\mathbf{k} \\ \mathcal{P}_\mathbf{k}^\dagger & -\mathcal{H}_\mathbf{k}^{QB} + \mu \mathbb{1}_{3\times 3} \end{pmatrix}, \tag{4.37}$$

with the chemical potential at the QBTP given by $\mu = 2t''$. Here, the pairing matrix is given by

$$\mathcal{P}_\mathbf{k} = \begin{pmatrix} 0 & \Delta_{\mathbf{k},x}^V & \Delta_{\mathbf{k},y}^V \\ \Delta_{-\mathbf{k},x}^V & 0 & \Delta_\mathbf{k}^W \\ \Delta_{-\mathbf{k},y}^V & \Delta_{-\mathbf{k}}^W & 0 \end{pmatrix}. \tag{4.38}$$

The parameters in this matrix are described by

$$\Delta_{\mathbf{k},\alpha}^V = \Delta_{+,\alpha}^V e^{ik_\alpha a/2} + \Delta_{-,\alpha}^V e^{-ik_\alpha a/2} \tag{4.39}$$

for $\alpha = x, y$, with spin-singlet order parameters, $\Delta_{\pm,\alpha}^V = V\langle \hat{s}_{\mathbf{j},\uparrow}\hat{s}_{\mathbf{j}\pm\mathbf{e}_\alpha/2,\downarrow} - \hat{s}_{\mathbf{j},\downarrow}\hat{s}_{\mathbf{j}\pm\mathbf{e}_\alpha/2,\uparrow}\rangle$. Here, $\mathbf{j}$ is a site from the A sublattice.

The order parameters generated from W can be expressed by using the NNN bond vectors. We recall that $\boldsymbol{\delta}_1 := (\mathbf{e}_x + \mathbf{e}_y)a/2$, $\boldsymbol{\delta}_2 := -(\mathbf{e}_x + \mathbf{e}_y)a/2$, $\boldsymbol{\delta}_3 := (\mathbf{e}_x - \mathbf{e}_y)a/2$, and $\boldsymbol{\delta}_4 := -(\mathbf{e}_x - \mathbf{e}_y)a/2$. In terms of these vectors, we have

55

$$\Delta_{\mathbf{k}}^{W} = \sum_{j=1}^{4} \Delta_{j}^{W} e^{i\mathbf{k}\cdot\boldsymbol{\delta}_{j}}, \tag{4.40}$$

with order parameters $\Delta_{i}^{W} = W\langle\hat{s}_{\mathbf{j},\uparrow}\hat{s}_{\mathbf{j}+\boldsymbol{\delta}_{i},\downarrow} - \hat{s}_{\mathbf{j},\downarrow}\hat{s}_{\mathbf{j}+\boldsymbol{\delta}_{i}}\rangle$ for $i = 1,...,4$. These RVB-type order parameters can conveniently be written in terms of the vectors

$$\boldsymbol{\Delta}^{V} = (\Delta_{+,x}^{V}, \Delta_{+,y}^{V}, \Delta_{-,x}^{V}, \Delta_{-,y}^{V}), \tag{4.41}$$

$$\boldsymbol{\Delta}^{W} = (\Delta_{1}^{W}, \Delta_{2}^{W}, \Delta_{3}^{W}, \Delta_{4}^{W}). \tag{4.42}$$

Notice that we have the same coefficients as in the non-interacting part in the Hamiltonian for vectors of the type $\sim (1,1,1,1)$, implying hidden order (no gap). If we allow for some other values, we see by a careful examination of the possible quasiparticle spectra that no gapped superfluid can form for any value of $\boldsymbol{\Delta}^{V}$. A particular choice of values for the order parameters can only change the curvature of the quasi-particle branches, see Figure 4.6(b). However, we find that it is possible to create a gap at zero energy with $\boldsymbol{\Delta}^{W}$. For example, this can be obtained by the combination of bond order parameters, given by $\boldsymbol{\Delta}^{W} \sim (1,0,0,0)$, see Figure 4.6(c). This means that in the RVB-pairing picture, we need NNN interactions to create a full superfluid gap for every point in the 1BZ. From this small discussion, it may be worthwhile to consider a more careful analysis from the problem that is posed here. This will be addressed in a future work.
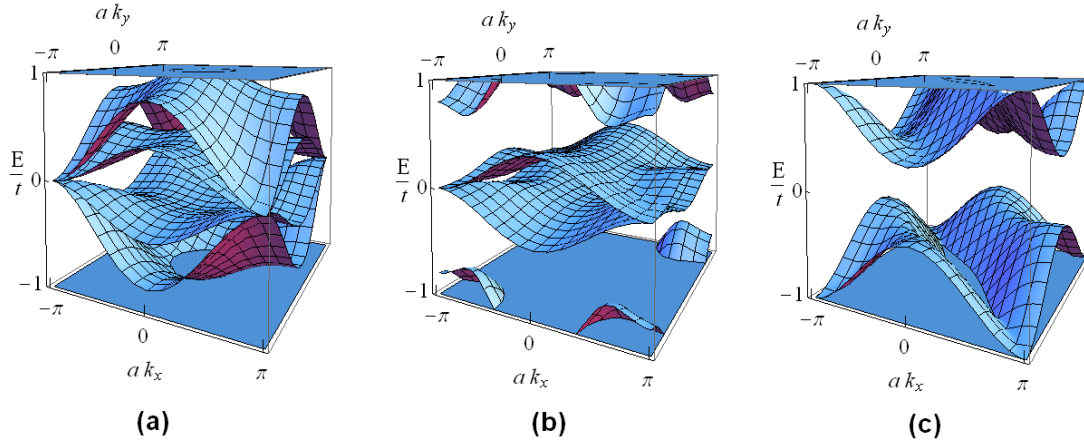
Figure 4.6: Effect of the RVB-type order parameters $\boldsymbol{\Delta}^{V}$ and $\boldsymbol{\Delta}^{W}$ on the quasiparticle spectrum around $E = 0$ for $\epsilon_{A} = -4t$, $\mu = 2t''$, and $t'' = 0.1t$. (a) If all the order parameters are chosen to be zero, then the spectrum is gapless at the M-point. (b) Choosing $\boldsymbol{\Delta}^{V} = (2t, 0, 0, 0)$ gaps out certain quasiparticle branches, but the system is still gapless at the M-point. (c) If the order parameters from the NNN attraction W are considered, it is possible to create a full gap everywhere in the 1BZ. The example that we give here is $\boldsymbol{\Delta}^{W} = (t, 0, 0, 0)$.

Chapter 5

Conclusion and outlook

In this thesis, we investigated two different subjects on the Lieb lattice: the QSHE and fermionic superfluidity. These two topics have been discussed in Chapter 3 and 4 respectively, while the prerequisites can be found in the first two chapters. For the QSHE problem, we have considered models that account for an intrinsic spin-orbit coupling, that on a lattice takes the form of a complex NNN hopping. We investigated how the topological features of such models are influenced by the conventional real NNN hopping contribution t'. As our main result, we have shown that t' may drive topological phase transitions in multigap systems, for which the helical edge states reverse direction. This change in the edge state spectrum can be understood from the spin Chern numbers of the bands that change value. Subsequently, we have calculated two phase diagrams that show the rich behaviour of these topological transitions. However, care must taken when interpreting these diagrams, because of the possible occurrence of negative indirect band gaps. This means that we have partially filled bands that give rise to a non-quantized contribution to the spin Hall conductivity, which may not be detected because the bulk is in this case a semi-metal.

The change in (spin) Chern numbers occurs because of specific band touchings in the 1BZ, for example by tilted anisotropic Dirac cones. Another important outcome of our studies is that it is possible to tune the momentum for which a band gap opens at these cones. It would thus be enlightening to look at this problem by the proposed classification of Juričić *et al.* [64], to see if dislocations can bind zero modes, and how this phenomenon depends on the positions of the Weyl cones in the 1BZ. Furthermore, it would be important to investigate how the two gaps that can occur between the three bands in the tight-binding spectrum, can be probed independently.

Finally, it would be interesting to see how the topological phase transitions are influenced when interactions are taken into account. We could, for example, consider spin- and charge density waves instabilities at the mean-field level. However, in a suitable parameter regime, there is still a large portion of the middle band that is flat. This means that interactions can become dominant over the kinetic terms, so that the system must be interpreted as strongly correlated. In this case, we could question the applicability of a mean-field approach.

The second subject that we discussed in this thesis is the problem of fermionic superfluidity on the Lieb lattice. Our philosophy here was to consider this problem in the weak coupling limit, where BCS-

like techniques could be applied. We added interactions to band structures that have a point-like Fermi surface for a suitable choice of the chemical potential. We investigated a particular type of Varma flux pattern and a quadratic band touching point that is formed by including third-nearest-neighbour hopping. In the first case, we find Weyl cones that are tunable, in sharp contrast to the protected position of the QBTP in the 1BZ. A critical interaction strength is needed to obtain a fermionic superfluid when the chemical potential is put at the Weyl points, while for the QBTP an infinitesimal attraction suffices. Despite these differences, these two situations have some features in common. For example, in both cases hidden order could be found: a fermionic superfluid that is gapless for specific points in the 1BZ. We saw that creating a full gap was especially difficult for longer-range types of attractive interactions, such as NN ones. However, for the on-site interaction, it is always possible to open a full gap for every point in the 1BZ.

The realization of fully gapped states may be particularly interesting for the occurrence of topological states of matter. For example, we could try to realize non-trivial states in the D or in the DIII classes, according to the classification that we discussed in Chapter 2. An NNN RVB-type order parameter for the QBTP may be the best candidate, because it may lead to a non-trivial superfluid state that is fully gapped. A competition with on-site pairing would also be interesting to pursue further. In addition, including higher orbitals, such as p, d and f may be important for realizing novel topological superfluids.

Finally, for the pairing in the Varma phase pattern, we have included the possibility of having an FFLO state by connecting two Weyl points that reside within the 1BZ. We have not considered the resulting spectrum of such a pairing in this thesis, nor have we considered the thermodynamically favored phases. However, it would certainly be interesting to look further into this problem and to compare the results with the proposal for graphene by Roy and Herbut [91]. In this setting, it would be worthwhile to investigate how topological excitations would manifest on the Lieb lattice, when such an FFLO state is present. Still, the apparent lack of symmetry in the Hamiltonian and the fact that the BdG matrix is relatively large makes this a non-trivial problem.

Acknowledgements

First of all I would like to thank my supervisor Cristiane de Morais Smith. Our meetings were always helpful and often very long: sometimes even for four hours without a break. I also appreciate the times that you corrected the work that I handed in. My co-supervisor Vladimir Juričić, I would also like to thank you for your insights in the various problems that concerned superconductivity and topological insulators. I would also like to thank my second co-supervisor Wouter Beugeling: your explanations were always very clear and thorough, and I really benefited from this on many occasions. Moreover, your knowledge of LaTeX was also very useful. Mark Goerbig is thanked for teaching me how to work with the Luttinger-Kohn representation and for our discussions about tilted Dirac cones. Henk Stoof, René van Roij and Rembert Duine are also thanked for helpful discussions. Furthermore, my gratitude goes to my family and friends for their support. My fellow students are thanked because they had to listen to my complaints when something did not work out. I think that Arie-Willem de Leeuw was the biggest victim in this regard. Charley Schaefer is thanked without a particular reason, just like you thanked me in your own master thesis without a reason. Finally, I would like to thank Suzan Gijsen. Su, I was always motivated by your support during a large portion of my thesis (although it was not always noticeable from my part). Anyways, I really appreciate it.

Appendix A

Eigenvectors of Hermitian 3×3 matrices

At several occasions in this thesis, we had to determine the eigenvalues of a Hermitian 3×3 matrix. For this the roots of a cubic polynomial had to be found, and the analytical expression for this are well-known. In this appendix, we will show that analytical expressions for the eigenvectors can also be found analytically very easily. It is a small trick that works, because we can take cross products for 3-vectors. However, this method is not always useful, because for complicated matrices, the expressions can become hard to handle. Moreover, the method can be prone to error propagation, so that it would not always be the most suitable method to use [94]. However, this method could be applied in Chapter 3, when we expressed the Chern number as a winding number in the case where $t' = 0$.

Let us begin with a Hermitian 3×3 matrix A, that satisfies $A^\dagger = A$. Suppose that $\mathbf{v}_i$ is an eigenvector, written as a column vector, with eigenvalue λ_i, which we assume to be non-degenerate for all $i = 1, 2, 3$. Since $\mathbf{v}_i$ is an eigenvector, we have that

$$(A - \lambda_i \mathbb{1})\mathbf{v}_i = O, \tag{A.1}$$

with O the 3×3 zero matrix. Taking the Hermitian conjugate of the above and multiplying it with the j-th unit vector $\mathbf{e}_j$, we find that

$$\mathbf{v}_i^* \cdot (A - \lambda_i \mathbb{1})\mathbf{e}_j = 0 \quad \forall j. \tag{A.2}$$

The above equation then tells us that $\mathbf{v}_i^*$ is perpendicular to every column of the matrix $A - \lambda_i \mathbb{1}$. Moreover, if the j-th column is linearly independent from the k-th column, we have that the normalized eigenvectors can be found by the formula

$$\mathbf{v}_i = \frac{[(A - \lambda_i \mathbb{1})\mathbf{e}_j \times (A - \lambda_i \mathbb{1})\mathbf{e}_k]^*}{||(A - \lambda_i \mathbb{1})\mathbf{e}_j \times (A - \lambda_i \mathbb{1})\mathbf{e}_k||}. \tag{A.3}$$

Bibliography

[1] N. P. Armitage, P. Fournier, and R. L. Greene, Rev. Mod. Phys. **82**, 2421 (2010).

[2] J. G. Bednorz and K. A. Müller, Z. Phys. B **64**, 189 (1986).

[3] C. E. Cough, M. S. Colcough, E. M. Forgan, R. G. Jordan, M. Keene, C. M. Muirhead, A. I. M. Rae, N. Thomas, J. S. Abell, and S. Sutton, Nature **326**, 855 (1987).

[4] J. Bardeen, L. N. Cooper, and J. R. Schrieffer, Phys. Rev. **108**, 1175 (1957).

[5] C. C. Tsuei, J. R. Kirtley, C. C. Chi, L. S. Yu-Jahnes, A. Gupta, T. Shaw, J. Z. Sun, and M. B. Ketchen, Phys. Rev. Lett. **73**, 593 (1994).

[6] E. W. Carlson, V. J. Emery, S. A. Kivelson, and D. Orgad, in *Superconductivity: Conventional and Unconventional Superconductors*, Vol. 1, edited by K. Bennemann and J. Ketterson (Springer, 2008) Chap. 21, p. 1227.

[7] H. R. Ott, in *Superconductivity: Conventional and Unconventional Superconductors*, Vol. 1, edited by K. Bennemann and J. Ketterson (Springer, 2008) Chap. 14, p. 765.

[8] E. Dagotto, Rev. Mod. Phys. **66**, 763 (1994).

[9] J. Zaanen, in *100 years of superconductivity*, edited by H. Rochalla and P. Kes (Chapman and Hall, 2010).

[10] J. Zaanen, G. A. Sawatzky, and J. W. Allen, Phys. Rev. Lett. **55**, 418 (1985).

[11] A. Damascelli, Z. Hussain, and Z.-X. Shen, Rev. Mod. Phys. **75**, 473 (2003).

[12] C. M. Varma, Phys. Rev. Lett. **83**, 3538 (1999).

[13] T. Timusk and B. Statt, Rep. Prog. Phys. **62**, 61 (1999).

[14] J. Orenstein and A. J. Millis, Science **288**, 468 (2000).

[15] M. R. Norman, H. Ding, M. Randeria, J. C. Capuzano, T. yokoya, T. Takeuchi, T. Takahashi, T. Mochiku, K. Kadowaki, P. Guptasarma, and D. G. Hinks, Nature **392**, 157 (1998).

[16] V. J. Emery and S. A. Kivelson, Nature **374**, 434 (1995).

[17] K. K. Gomes, A. N. Pasupathy, A. Pushp, S. Ono, Y. Ando, and A. Yazdani, Nature **447**, 569 (2007).

[18] R. A. L. Jones, *Soft Condensed Matter* (Oxford University Press, 2002).

[19] J. Zaanen and O. Gunnarsson, Phys. Rev. B **40**, 7391 (1989).

[20] A. H. Castro Neto and C. Morais Smith, in *Strong Interactions in Low Dimensions*, edited by D. Baeriswyl and L. Degiorgi (Kluwer Acad. Pub. Dordrecht, 2004) Chap. 9, p. 277.

[21] P. W. Anderson, Science **235**, 1196 (1987).

[22] N. D. Mermin and H. Wagner, Phys. Rev. Lett. **17**, 1133 (1966).

[23] P. C. Hohenberg, Phys. Rev. **158**, 383 (1967).

[24] V. J. Emery, Phys. Rev. Lett. **58**, 2794 (1987).

[25] M. H. Fischer and E. Kim, "Mean-field analysis of intra-unit-cell order in the emery model of the CuO_2 plane," (2011), arXiv:1106.6060 .

[26] F. C. Zhang and T. M. Rice, Phys. Rev. B **37**, 3759 (1988).

[27] I. Affleck and J. B. Marston, Phys. Rev. B **37**, 3774 (1988).

[28] G. Kotliar, Phys. Rev. B **37**, 3664 (1988).

[29] J. B. Marston and I. Affleck, Phys. Rev. B **39**, 11538 (1989).

[30] T. C. Hsu, J. B. Marston, and I. Affleck, Phys. Rev. B **43**, 2866 (1991).

[31] P. A. Lee, N. Nagaosa, and X.-G. Wen, Rev. Mod. Phys. **78**, 17 (2006).

[32] C. Nayak, Phys. Rev. B **62**, 4880 (2000).

[33] S. Chakravarty, R. B. Laughlin, D. K. Morr, and C. Nayak, Phys. Rev. B **63**, 094503 (2001).

[34] C. M. Varma, Phys. Rev. B **73**, 155113 (2006).

[35] B. Fauqué, Y. Sidis, V. Hinkov, S. Pailhès, C. T. Lin, X. Chaud, and P. Bourges, Phys. Rev. Lett. **96**, 197001 (2006).

[36] J. Xia, E. Schemm, G. Deutscher, S. A. Kivelson, D. A. Bonn, W. N. Hardy, R. Liang, W. Siemons, G. Koster, M. M. Fejer, and A. Kapitulnik, Phys. Rev. Lett. **100**, 127002 (2008).

[37] K. Sun and E. Fradkin, Phys. Rev. B **78**, 245122 (2008).

[38] Y. He, J. Moore, and C. M. Varma, Phys. Rev. B **85**, 155106 (2012).

[39] C. Weeks and M. Franz, Phys. Rev. B **82**, 085310 (2010).

[40] X.-L. Qi and S.-C. Zhang, Rev. Mod. Phys. **83**, 1057 (2011).

[41] M. Z. Hasan and C. L. Kane, Rev. Mod. Phys. **82**, 3045 (2010).

[42] K. v. Klitzing, G. Dorda, and M. Pepper, Phys. Rev. Lett. **45**, 494 (1980).

[43] T. Ando, Y. Matsumoto, and Y. Uemura, J. Phys. Soc. Jpn. **39**, 279 (1975).

[44] M. Goerbig, "Quantum hall effects," Les Houches Summer School (2009).

[45] R. B. Laughlin, Phys. Rev. Lett. **50**, 1395 (1983).

[46] D. J. Thouless, M. Kohmoto, M. P. Nightingale, and M. den Nijs, Phys. Rev. Lett. **49**, 405 (1982).

[47] M. V. Berry, Proc. R. Soc. Lond. A **392**, 45 (1984).

[48] D. Xiao, M.-C. Chang, and Q. Niu, Rev. Mod. Phys. **82**, 1959 (2010).

[49] M. Kohmoto, Annals of Physics **160**, 343 (1985).

[50] F. D. M. Haldane, Phys. Rev. Lett. **61**, 2015 (1988).

[51] C. L. Kane and E. J. Mele, Phys. Rev. Lett. **95**, 146802 (2005).

[52] C. L. Kane and E. J. Mele, Phys. Rev. Lett. **95**, 226801 (2005).

[53] M. König, S. Wiedmann, C. Brüne, A. Roth, H. Buhmann, L. W. Molenkamp, X.-L. Qi, and S.-C. Zhang, Science **318**, 766 (2007).

[54] B. A. Bernevig, T. L. Hughes, and S.-C. Zhang, Science **314**, 1757 (2006).

[55] C. Bena and G. Montambaux, New Journal of Physics **11**, 095003 (2009).

[56] H. A. Kramers, Proc. Amsterdam Acad. **33**, 959 (1930).

[57] W. Beugeling, *Topological states of matter in two-dimensional fermionic systems*, Ph.D. thesis, Utrecht University (2012).

[58] L. Fu, C. L. Kane, and E. J. Mele, Phys. Rev. Lett. **98**, 106803 (2007).

[59] A. Kitaev, AIP Conf. Proc. **1134**, 22 (2009).

[60] S. Ryu, A. P. Schnyder, A. Furusaki, and A. W. W. Ludwig, New Journal of Physics **12**, 065010 (2010).

[61] A. P. Schnyder, S. Ryu, and A. W. W. Ludwig, Phys. Rev. Lett. **102**, 196804 (2009).

[62] A. P. Schnyder and S. Ryu, Phys. Rev. B **84**, 060504 (2011).

[63] X.-L. Qi, T. L. Hughes, S. Raghu, and S.-C. Zhang, Phys. Rev. Lett. **102**, 187001 (2009).

[64] V. Juričić, A. Mesaros, R.-J. Slager, and J. Zaanen, Phys. Rev. Lett. **108**, 106403 (2012).

[65] I. Bloch, J. Dalibard, and W. Zwerger, Rev. Mod. Phys. **80**, 885 (2008).

[66] M. P. A. Fisher, P. B. Weichman, G. Grinstein, and D. S. Fisher, Phys. Rev. B **40**, 546 (1989).

[67] D. Jaksch, C. Bruder, J. I. Cirac, C. W. Gardiner, and P. Zoller, Phys. Rev. Lett. **81**, 3108 (1998).

[68] M. Greiner, O. Mandel, T. Esslinger, T. W. Hänsch, and I. Bloch, Nature **415**, 39 (2002).

[69] V. Apaja, M. Hyrkäs, and M. Manninen, Phys. Rev. A **82**, 041402 (2010).

[70] R. Shen, L. B. Shao, B. Wang, and D. Y. Xing, Phys. Rev. B **81**, 041410 (2010).

[71] J. H. Shirley, Phys. Rev. **138**, B979 (1965).

[72] A. Eckardt, C. Weiss, and M. Holthaus, Phys. Rev. Lett. **95**, 260404 (2005).

[73] M. Di Liberto, O. Tieleman, V. Branchina, and C. Morais Smith, Phys. Rev. A **84**, 013607 (2011).

[74] N. Goldman, J. Beugnon, and F. Gerbier, Phys. Rev. Lett. **108**, 255303 (2012).

[75] M. Buchhold, D. Cocks, and W. Hofstetter, Phys. Rev. A **85**, 063614 (2012).

[76] W. Beugeling, J. C. Everts, and C. Morais Smith, "Topological phase transitions induced by next-nearest-neighbor hopping in two-dimensional lattices," (2012), arXiv:1207.6545 .

[77] H. Nielsen and M. Ninomiya, Nucl. Phys. B **185**, 20 (1981).

[78] E. Dagotto, E. Fradkin, and A. Moreo, Phys, Lett. B **172**, 383 (1986).

[79] D. Green, L. Santos, and C. Chamon, Phys. Rev. B **82**, 075104 (2010).

[80] D. N. Sheng, Z. Y. Weng, L. Sheng, and F. D. M. Haldane, Phys. Rev. Lett. **97**, 036808 (2006).

[81] J. M. Luttinger and W. Kohn, Phys. Rev. **97**, 869 (1955).

[82] M. O. Goerbig, J.-N. Fuchs, G. Montambaux, and F. Piéchon, Phys. Rev. B **78**, 045415 (2008).

[83] D. Makogon, I. B. Spielman, and C. Morais Smith, EPL **97**, 33002 (2012).

[84] T. Fukui, Y. Hatsugai, and H. Suzuki, J. Phys. Soc. Jpn. **74**, 1674 (2005).

[85] F. D. M. Haldane, Phys. Rev. Lett. **93**, 206602 (2004).

[86] W. Tsai, C. Fang, H. Yao, and J. Hu, "Interaction-driven topological and nematic phases on the lieb lattice," (2011), arXiv:1112.5789 .

[87] O. Tieleman, A. Lazarides, and C. Morais Smith, Phys. Rev. A **83**, 013627 (2011).

[88] L.-K. Lim, A. Lazarides, A. Hemmerich, and C. Morais Smith, Phys. Rev. A **82**, 013616 (2010).

[89] B. Uchoa and A. H. Castro Neto, Phys. Rev. Lett. **98**, 146801 (2007).

[90] A. M. Black-Schaffer and S. Doniach, Phys. Rev. B **75**, 134512 (2007).

[91] B. Roy and I. F. Herbut, Phys. Rev. B **82**, 035429 (2010).

[92] P. Fulde and R. A. Ferrell, Phys. Rev. **135**, A550 (1964).

[93] A. I. Larkin and Y. N. Ovchinnikov, Zh. Eksp. Teor. Fiz. **47**, 1136 (1964).

[94] J. Kopp, Int. J. Mod. Phys. C **19**, 523 (2008).